This is the author's version of an article published in the IEEE Transactions on Robotics (T-RO).
The final published paper can be found at DOI: 10.1109/TRO.2024.3366818

Data-driven Momentum Observers with Physically Consistent Gaussian Processes

Giulio Evangelisti and Sandra Hirche

***Abstract*—This article proposes a data-driven modeling framework with physically consistent Gaussian Processes (GPs), enabling learning-based disturbance estimation for uncertain mechanical systems with covariance-adaptive Momentum Observers (MOs). We present novel error bound results in closed form, holding with high, exactly computable probabilities, and exploit the multidimensional, physically constrained function distribution induced by the differential equation structure of Lagrangian systems. The inherent uncertainty quantification provided by GPs and the derived model error bounds are then leveraged to probabilistically guarantee exponential stability of a class of data-driven, adaptive MOs with user-definable convergence parameters. We demonstrate the performance of our proposed methods in simulations and physical experiments, showing significant improvements compared to the state-of-the-art from industry and research.**

***Index Terms*—Gaussian processes, learning and adaptive systems, probability and statistical methods, model learning for control.**

I. Introduction

With the emergence of increasingly complex physical systems for a variety of manipulation [1] and cooperation [2] tasks, and their deployment in increasingly uncertain environments, accurate modeling, control, and estimation are crucial yet more challenging. Particularly in the fields of soft, variable impedance, and rehabilitation robotics [3]–[5], dynamic interactions not only become nonnegligible but are explicitly desired and accounted for by design, enabling new applications and possibilities [6]. Thus, the demand for providing reliable and accurate information on the nature of environmental interactions is steadily rising [7]. At the same time, performances of model-based control and observation techniques become critically dependent on precise system knowledge, such as in, e.g., whole-bodied control of legged robots [8], dynamic control of soft robots [9], human-robot interaction [10], or collision estimation [11].

We address these issues by data-driven modeling with Lagrangian-Gaussian Processes (L-GPs), which are constrained to respect the relevant physical laws of our targeted class of mechanical systems. For the estimation of external forces, we leverage the physical consistency of our learning-based model, allowing a natural embedding into the structure of Momentum Observers (MOs) [12], [13]. Attributed to their linear error dynamics, independence of accelerations and force directions, and avoidance of inverting the mass-inertia matrix, MOs have been shown to be the best-performing method for rigid-bodied robots [11]. However, due to their formulation based on the generalized momentum as a nonmeasurable output, they are still critically dependent on exact models and, particularly, the inertia matrix.

In physics-informed machine learning, these same limitations, revolving around uncertain momentum and inertia, are also present in a variety of proposed methods, which are either based on Hamiltonian models with GPs and neural networks [14]–[17] or on exact knowledge of the mass-inertia matrix [18]–[20]. In general, the notion of combining rigid-body mechanics with data-driven modeling techniques holds great promise for the control and observation of uncertain robotic systems, improving data efficiency and reliability via their physical integrity [21]. Also traditional parametric identification techniques [22] profit from enforcing physical consistency [23], [24] but are limited to dynamical systems with low complexity since they require rigidity and thus, linearity in the parameters. Especially for soft-bodied robots, developing reliable yet tractable models is still a crucial ongoing issue [9], [25].

Supervised learning techniques using GPs have become increasingly popular due to their fundamental data efficiency [26] and inherent uncertainty quantification [27]. Additionally, GPs enable the derivation of prediction error bounds [28], which can be used to provide stability guarantees for a large number of control laws such as feedback linearization [29], tracking [30], or robust [31], control. Moreover, their stochastic construction closely relates them to Kalman filters [32], lending them a measure of optimality for estimation. In general, GPs do not account for physical consistency, however. An approach based on vector-valued Reproducing Kernel Hilbert Spaces (RKHS) is proposed in [33], using kernel regression for the Lagrangian, but does not provide any further structure or guarantees. Incorporating variational integrators into GP-based learning can be advantageous when long-time numerical integration is of interest, as shown in [34]. However, the energy structuring of the Lagrangian and its quadratic forms are not considered, prohibiting an application to most physical model-based control or observation methods.

In the context of disturbance observation, few data-driven approaches have been proposed thus far. Long Short-Term Memory (LSTM) networks are used in [35] to estimate the external torque without giving any guarantees, some relying on a parallel MO for a residual-based estimate [36]. A work with similar goals to ours is proposed in [37], combining standard GPs with piecewise constant curvature (PCC) models [9] into

Both authors are with the Chair of Information-oriented Control, TUM School of Computation, Information and Technology, Technical University of Munich, 80333 Munich, Germany (e-mail: g.evangelisti, hirche@tum.de).

Manuscript received August 3, 2023; revised December 7, 2023; accepted February 9, 2024.

a disturbance observer for soft robots. However, the authors neglect Coriolis and mass-inertia forces and do not provide closed-form results for convergence rate or steady-state error. To the best of our knowledge, GPs have yet to be applied to data-driven MOs, along with physically consistent learning to disturbance observation in general. Moreover, error bound results for GPs [28], [30], [38], [39] until now have only considered scalar functions, assume bounded observation noise, neglect multidimensional function correlations, or suffer from strong conservatism [40] due to probabilistic approximations.

A. Contribution

The main contribution of this article is the integration of physically consistent L-GPs into a class of uncertainty-adaptive, proportional (P) and proportional-derivative (PD) gain MOs. Thus, we enable reliable learning-based estimation of external forces acting on uncertain mechanical systems. Compact exponential stability guarantees are provided based on the formulation of novel prediction error bounds for GPs, allowing user-definable convergence parameters. Theory and methods are validated in numerical simulations and physical experiments. In particular, comparisons with the state-of-the-art from disturbance observation, error bounds, and modeling and identification methods show significant improvements on both theoretical and practical levels. Additionally, we extend the applicability of the L-GP model, first proposed in our previous work [41], from conservative to dissipative systems.

B. Notation

Vectors $\boldsymbol{a}$ and matrices $\boldsymbol{A}$ are denoted with bold lower and upper case characters, respectively. $\boldsymbol{I}$ denotes the identity, $\mathbf{0}$ the zero and $\mathbf{1}$ the ones matrix. $\mathrm{E}[\cdot]$ and $\mathrm{Var}[\cdot]$ denote the expectation and variance operators, $\bar{\lambda}(\cdot)$ and $\underline{\lambda}(\cdot)$ the maximal and minimal eigenvalues, $\mathbb{R}$ and $\mathbb{N}$ the set of real and natural numbers, respectively, $|\cdot|$ the cardinality of a set, $\mathcal{N}(\boldsymbol{\mu}, \boldsymbol{\Sigma})$ a multivariate Gaussian distribution with mean $\boldsymbol{\mu}$ and covariance $\boldsymbol{\Sigma}$, and $\|\cdot\|$ the Euclidian norm if not stated otherwise. The operator $\mathrm{vec}(\cdot)$ stacks the columns of a matrix to form a vector. Finally, $\gamma(n)$, $\gamma(n+1/2)$ and $\Gamma_n(\rho)$ denote the ordinary and incomplete (upper) gamma functions

$$\gamma(n) = (n-1)!\,, \quad \gamma(n+\tfrac{1}{2}) = \tfrac{(2n)!}{4^n n!}\sqrt{\pi}\,, \tag{1a}$$

$$\Gamma_n(\rho) = \int_{\rho}^{\infty} r^{n-1} e^{-r} dr\,, \tag{1b}$$

evaluated at positive and nonnegative integer n, respectively, and radius $\varrho \in \mathbb{R}^+$.

C. Physical Consistency and Euler-Lagrange Systems

Throughout this work, we will implicitly refer to the following model classification.

Definition 1 (Physical Consistency): A model is called physically consistent if it is constrained to respect the physical laws relevant to its modeling level.

A typical example of physical consistency for rigid-body models is an inertial parameter set with positive mass and positive definite inertia tensor satisfying the triangle inequalities [23]. For finite-dimensional models of non-rigid bodies, these parameters become state-dependent, and thus, a higher modeling level respecting the fundamental characteristics of Lagrangian systems [42] is required. In particular, trajectories must satisfy the Euler-Lagrange (EL) equations in accordance with Hamilton's principle of Least Action, and conservative forces must be derivable from potentials [43]. Note that an exact model for elastic bodies necessarily leads to infinite dimensionality [44]. A further classification into analytical and probabilistic [41], or physical semi-consistency [23], is also possible.

In this article, we assume the uncertain dynamics of Euler-Lagrange (EL) systems with equations of motion [45]

$$\boldsymbol{M}(\boldsymbol{q})\ddot{\boldsymbol{q}} + \boldsymbol{C}(\boldsymbol{q},\dot{\boldsymbol{q}})\dot{\boldsymbol{q}} + \boldsymbol{g}(\boldsymbol{q}) + \boldsymbol{\tau}_f = \boldsymbol{\tau}_m + \boldsymbol{\tau}_{\text{ext}} = \boldsymbol{\tau}\,, \tag{2}$$

where $\boldsymbol{q} \in \mathbb{R}^N$ is the set of generalized coordinates, $\boldsymbol{M}(\boldsymbol{q}) \in \mathbb{R}^{N\times N}$ the (symmetric) positive definite, inertia matrix, $\boldsymbol{C}(\boldsymbol{q},\dot{\boldsymbol{q}}) \in \mathbb{R}^{N\times N}$ the generalized Coriolis matrix such that $\dot{\boldsymbol{M}} - 2\boldsymbol{C}$ is skew-symmetric, and the vector of generalized potential forces $\boldsymbol{g}(\boldsymbol{q}) \coloneqq \frac{\partial}{\partial \boldsymbol{q}} V$ derived from the potential energy $V(\boldsymbol{q}) \in \mathbb{R}$. The nonconservative torques $\boldsymbol{\tau}_f$, $\boldsymbol{\tau}_m$, and $\boldsymbol{\tau}_{\text{ext}}$ represent the dissipative friction, active motor actuation, and external joint torques, respectively.

II. Modeling Framework: Lagrangian-Gaussian Processes (L-GPs)

In this section, we propose a framework for data-driven modeling of mechanical systems with physically consistent Gaussian Processes (GPs), including, but not limited to, the dynamics of rigid bodies derivable via classical mechanics [43]. To begin with, we provide a brief overview of GPs based on [27]. For a complete introduction, the reader is referred to the literature [46]–[48].

A. Gaussian Processes (GPs)

A Gaussian Process (GP) is a stochastic process extending the Gaussian probability distribution from random variables to functions. Therefore, it inherits the convenient properties of the Normal distribution, such that, in particular, conditioning and marginalization of any finite realization remains Gaussian. For $\boldsymbol{x}, \boldsymbol{x}' \in \mathcal{X}$ in a continuous domain $\mathcal{X} \subseteq \mathbb{R}^M$, a GP with mean $\boldsymbol{m}(\boldsymbol{x})$ and covariance or kernel $\boldsymbol{K}(\boldsymbol{x}, \boldsymbol{x}')$ is denoted by

$$\boldsymbol{f}(\boldsymbol{x}) \sim \mathcal{GP}\left(\boldsymbol{m}(\boldsymbol{x}), \boldsymbol{K}(\boldsymbol{x}, \boldsymbol{x}')\right)\,, \tag{3}$$

where we consider vector-valued functions $\boldsymbol{f}\colon \mathbb{R}^M \to \mathbb{R}^N$. The kernel matrix $\boldsymbol{K}(\boldsymbol{x}, \boldsymbol{x}') \in \mathbb{R}^{N\times N}$ is positive semidefinite [48] for any $\boldsymbol{x}, \boldsymbol{x}'$, quantifying the correlation or similarity between the components of $\boldsymbol{f}(\boldsymbol{x})$ and $\boldsymbol{f}(\boldsymbol{x}')$, and also determining higher-level functional properties such as smoothness. It is parametrized by so-called hyperparameters, mostly optimized numerically via the marginal likelihood [27] to maximize the probability of observing the measured outputs.

Consider now D observations $\boldsymbol{Y} \in \mathbb{R}^{N\times D}$ at locations $\boldsymbol{X} \in \mathbb{R}^{M\times D}$ perturbed by white noise $\boldsymbol{\epsilon}$ according to

$$\boldsymbol{y}_i = \boldsymbol{f}(\boldsymbol{x}_i) + \boldsymbol{\epsilon}_i\,, \quad \boldsymbol{\epsilon}_i \sim \mathcal{N}(\mathbf{0}, \boldsymbol{\Sigma}_{\boldsymbol{\epsilon}_i})\,, \quad i = 1, \dots, D\,. \tag{4}$$

Most simply, the covariance $\boldsymbol{\Sigma}_{\boldsymbol{\epsilon}_i}$ is a scaled identity matrix $\boldsymbol{\Sigma}_{\boldsymbol{\epsilon}_i} = \sigma_{\boldsymbol{\epsilon}}^2 \boldsymbol{I}$, representing the case of scalar i.i.d. noise processes with the same variance $\sigma_{\boldsymbol{\epsilon}}^2$ disturbing each measurement component. For regression, GPs then exploit the joint Gaussian distribution of the measurements $\boldsymbol{Y}$ and a desired estimate $\boldsymbol{f}(\boldsymbol{x})$ by conditioning on the former, leading to the posterior mean $\boldsymbol{\mu_f}(\boldsymbol{x}) \equiv \mathrm{E}[\boldsymbol{f}(\boldsymbol{x})|\boldsymbol{Y}, \boldsymbol{X}]$ and covariance $\boldsymbol{\Sigma_f}(\boldsymbol{x}) \equiv \mathrm{Var}[\boldsymbol{f}(\boldsymbol{x})|\boldsymbol{Y}, \boldsymbol{X}]$ given analytically by

$$\boldsymbol{\mu_f}(\boldsymbol{x}) = \boldsymbol{m}(\boldsymbol{x}) + \boldsymbol{K}(\boldsymbol{x}, \boldsymbol{X})\big(\boldsymbol{K}(\boldsymbol{X},\boldsymbol{X}) + \boldsymbol{\Sigma_\epsilon}\big)^{-1}\mathrm{vec}(\boldsymbol{Y} - \boldsymbol{m}(\boldsymbol{X})),$$
$$\boldsymbol{\Sigma_f}(\boldsymbol{x}) = \boldsymbol{K}(\boldsymbol{x}, \boldsymbol{x}) - \boldsymbol{K}(\boldsymbol{x}, \boldsymbol{X})\big(\boldsymbol{K}(\boldsymbol{X}, \boldsymbol{X}) + \boldsymbol{\Sigma_\epsilon}\big)^{-1}\boldsymbol{K}(\boldsymbol{X}, \boldsymbol{x}),$$

where $\boldsymbol{K}(\boldsymbol{X}, \boldsymbol{X})$ and $\boldsymbol{\Sigma_\epsilon}$ are ND times ND block matrices denoting the multidimensional Gramian and noise covariance, respectively.

Moreover, GPs have the key property that linear transformations remain GPs [46] due to their stochastic construction based on the expectation. Thus, applying a transformation operator $\mathcal{T}_{\boldsymbol{x}}$ which is linear, such as differentiation or integration, to (3), results in another GP given by

$$\mathcal{T}_{\boldsymbol{x}} \boldsymbol{f}(\boldsymbol{x}) \sim \mathcal{GP}\left(\mathcal{T}_{\boldsymbol{x}} \boldsymbol{m}(\boldsymbol{x}), \mathcal{T}_{\boldsymbol{x}} \boldsymbol{K}(\boldsymbol{x}, \boldsymbol{x}') \mathcal{T}_{\boldsymbol{x}'}^\top\right). \tag{5}$$

For the transformation of the covariance, $\mathcal{T}_{\boldsymbol{x}'}^\top$ is here applied from the right to yield an exterior product [49]. Consider for instance a scalar process $g(\boldsymbol{x}) \sim \mathcal{GP}\left(m_g(\boldsymbol{x}), k_g(\boldsymbol{x}, \boldsymbol{x}')\right)$. Then, taking the gradient $\frac{\partial g}{\partial \boldsymbol{x}}$ induces a multidimensional GP according to (3) with mean vector $\boldsymbol{m}$ and kernel matrix $\boldsymbol{K}$ given by the gradient of m_g w.r.t. $\boldsymbol{x}$ and the (Sub-)Hessian of k_g w.r.t. $(\boldsymbol{x}, \boldsymbol{x}')$, such that

$$\tfrac{\partial g(\boldsymbol{x})}{\partial \boldsymbol{x}} \sim \mathcal{GP}\left(\tfrac{\partial m_g(\boldsymbol{x})}{\partial \boldsymbol{x}}, \tfrac{\partial^2 k_g(\boldsymbol{x}, \boldsymbol{x}')}{\partial \boldsymbol{x} \partial \boldsymbol{x}'}\right).$$

Having introduced the underlying concepts of GPs, we now describe our modeling scheme, aiming to unify the data-driven probabilistic framework of GPs with first-order principles from physics. Based on [41], we extend the method's applicability from conservative to dissipative systems, thus making up our first contribution.

B. Physically Consistent Learning of Mechanical Systems with Lagrangian-Gaussian Processes (L-GPs)

The core concept of our proposed model is to constrain the function space of the employed GP distribution to be maximally physically consistent. Firstly, we leverage the operator

$$\mathcal{L}_{\boldsymbol{q}} \coloneqq \left(\tfrac{\partial}{\partial \dot{\boldsymbol{q}}^\top} \ddot{\boldsymbol{q}} + \tfrac{\partial}{\partial \boldsymbol{q}^\top} \dot{\boldsymbol{q}}\right) \tfrac{\partial}{\partial \dot{\boldsymbol{q}}} - \tfrac{\partial}{\partial \boldsymbol{q}} \tag{6}$$

to deterministically satisfy Hamilton's principle of Least Action by embedding the differential equation structure of conservative Euler-Lagrange (EL) systems [43]

$$\tfrac{d}{dt} \tfrac{\partial L}{\partial \dot{\boldsymbol{q}}} - \tfrac{\partial L}{\partial \boldsymbol{q}} = \boldsymbol{\tau}_c = \mathcal{L}_{\boldsymbol{q}} L(\boldsymbol{q}, \dot{\boldsymbol{q}}) \tag{7}$$

into the model (3). Then, asserting for the unknown Lagrangian function $L(\boldsymbol{q}, \dot{\boldsymbol{q}})$ a scalar GP with mean m_L, kernel k_L, and applying the linear transformation (6), we obtain

$$\boldsymbol{\tau}_c(\boldsymbol{x}) \sim \mathcal{GP}\left(\mathcal{L}_{\boldsymbol{q}} m_L(\boldsymbol{q}, \dot{\boldsymbol{q}}), \mathcal{L}_{\boldsymbol{q}} \mathcal{L}_{\boldsymbol{q}'}^\top k_L(\boldsymbol{q}, \dot{\boldsymbol{q}}, \boldsymbol{q}', \dot{\boldsymbol{q}}')\right) \tag{8}$$

due to (5) for $\boldsymbol{x} = (\boldsymbol{q}, \dot{\boldsymbol{q}}, \ddot{\boldsymbol{q}})$.

Secondly, assuming the dissipative component to consist of viscous, Coulomb, and dry-contact [50] frictional effects

$$\boldsymbol{\tau}_f = \boldsymbol{D}_v(\dot{\boldsymbol{q}}) \dot{\boldsymbol{q}} + \boldsymbol{D}_d(\dot{\boldsymbol{q}}) \boldsymbol{h}(\dot{\boldsymbol{q}}), \tag{9}$$

where $\boldsymbol{D}_v, \boldsymbol{D}_d \succeq \boldsymbol{0}$ and $\boldsymbol{h}(\dot{\boldsymbol{q}}) = \arctan(d_s \dot{\boldsymbol{q}})$, $d_s \gg 1$, we model the total $\boldsymbol{\tau}$ as a multidimensional composite GP

$$\boldsymbol{\tau} = \boldsymbol{\tau}_c + \boldsymbol{\tau}_f \sim \mathcal{GP}\left(\mathcal{L}_{\boldsymbol{q}} m_L + \boldsymbol{m}_f, \mathcal{L}_{\boldsymbol{q}} \mathcal{L}_{\boldsymbol{q}'}^\top k_L + \boldsymbol{K}_f\right) \tag{10}$$

with prior $\boldsymbol{m}_f$ on (9) and the dissipative covariance

$$\boldsymbol{K}_f = \mathrm{diag}(\dot{\boldsymbol{q}}) \boldsymbol{K}_v \mathrm{diag}(\dot{\boldsymbol{q}}') + \mathrm{diag}(\boldsymbol{h}(\dot{\boldsymbol{q}})) \boldsymbol{K}_d \mathrm{diag}(\boldsymbol{h}(\dot{\boldsymbol{q}}')). \tag{11}$$

In the simplest case, $\boldsymbol{D}_v, \boldsymbol{D}_d$ and therefore also the kernel matrices $\boldsymbol{K}_v, \boldsymbol{K}_d$ are diagonal, resulting in N scalar independent GPs each for the respective friction coefficients. Also, note that the damping matrices in (9) and accordingly also the kernels in (11) can straightforwardly be extended to include dependencies on the position $\boldsymbol{q}$.

Finally, the Lagrangian in (7)–(8) is split up into its energy components $L = T - G - U$ with the kinetic energy $T(\boldsymbol{q}, \dot{\boldsymbol{q}})$ as well as the gravitational and elastic potentials $G(\boldsymbol{q})$ and $U(\boldsymbol{q})$, respectively, for each of which we consider a separate independent GP. In particular, for the kinetic energy, we make use of a specific kernel structure [41] given by

$$k_T = \frac{1}{4} \dot{\boldsymbol{q}}^\top \mathrm{diag}(\dot{\boldsymbol{q}}') \boldsymbol{\Theta}_{\boldsymbol{M}}(\boldsymbol{q}, \boldsymbol{q}') \mathrm{diag}(\dot{\boldsymbol{q}}') \dot{\boldsymbol{q}} \tag{12}$$

with the Cholesky decomposed covariance $\boldsymbol{\Theta}_{\boldsymbol{M}} = \boldsymbol{R}_{\boldsymbol{M}}^\top \boldsymbol{R}_{\boldsymbol{M}}$ and upper-right triangular $\boldsymbol{R}_{\boldsymbol{M}}(\boldsymbol{q}, \boldsymbol{q}')$. The elastic energy GP $U(\boldsymbol{q})$ is constrained analogously.

As a consequence of the structures (7)–(12), the posterior $\hat{\boldsymbol{\tau}} \coloneqq \boldsymbol{\mu_\tau}$ of the dissipative L-GP (10) can be written as

$$\hat{\boldsymbol{\tau}}(\boldsymbol{x}) = \hat{\boldsymbol{M}}(\boldsymbol{q}) \ddot{\boldsymbol{q}} + \hat{\boldsymbol{C}}(\boldsymbol{q}, \dot{\boldsymbol{q}}) \dot{\boldsymbol{q}} + \hat{\boldsymbol{g}}(\boldsymbol{q}) + \hat{\boldsymbol{\tau}}_f(\dot{\boldsymbol{q}}). \tag{13}$$

Here, $\hat{\boldsymbol{M}} \colon \mathbb{R}^N \to \mathbb{R}^{N \times N}$ is the symmetric posterior mass-inertia estimate, guaranteed to be positive definite with high probability [41], and $\hat{\boldsymbol{C}}$ is the Coriolis estimate constructed as $\hat{\boldsymbol{C}}(\boldsymbol{q}, \dot{\boldsymbol{q}}) \coloneqq \frac{1}{2}\left(\frac{\partial^2 \hat{T}}{\partial \dot{\boldsymbol{q}} \partial \boldsymbol{q}^\top} + \dot{\hat{\boldsymbol{M}}}(\boldsymbol{q}) - \frac{\partial^2 \hat{T}}{\partial \boldsymbol{q} \partial \dot{\boldsymbol{q}}^\top}\right)$ [45]. These first two terms, combined with the potential force estimate $\hat{\boldsymbol{g}}(\boldsymbol{q}) = \frac{\partial}{\partial \boldsymbol{q}}(\hat{G} + \hat{U})$, also comprise the posterior $\hat{\boldsymbol{\tau}}_c \coloneqq \boldsymbol{\mu}_{\boldsymbol{\tau}_c}$ of the conservative torque GP (8), and are deterministically guaranteed to be lossless [41], due to the differential structural embedding (7) and the skew-symmetry of $\dot{\hat{\boldsymbol{M}}} - 2\hat{\boldsymbol{C}}$.

Remark 1: The mass-inertia estimate $\hat{\boldsymbol{M}}$ is a matrix-valued GP which is physically consistent since it probabilistically preserves positive definiteness and constrains the function space of the kinetic energy to quadratic forms; see Appendix E for an RKHS derivation. No further restriction is imposed on its components; in particular, no dependency on constant inertial parameters is enforced, as is well-known to hold for rigid bodies via the linear combination of body Jacobians and generalized parametric inertia matrices [45]. Thus, the L-GP guarantees physical consistency probabilistically for rigid-body systems and deterministically for EL systems (7).

III. Multidimensional Model Error Bounds

Essentially, the described model in section II-B is physically consistent yet still data-driven and, therefore, affected by measurement disturbances due to, e.g., noise. For the safe application of any model-based controller or observer, the model error must be analyzed and ideally shown to be bounded to guarantee stable closed-loop dynamics. GPs naturally enable the quantification of uncertainty in the model through their stochastic framework. In this section, we build on this property and present a series of novel error bound results. We require the following probabilistic condition to be fulfilled.

Assumption 1: The unknown vector-valued function $\boldsymbol{f}(\boldsymbol{x})$ is drawn from a GP according to (3) of which $D \in \mathbb{N}$ noisy observations have been collected according to (4).

The restrictiveness of this assumption depends on the kernel $\boldsymbol{K}(\boldsymbol{x}, \boldsymbol{x}')$ in (3) since it defines the space of functions which can be represented according to Mercer's decomposition theorem [51]. For instance, diagonal covariances consisting of scalar universal [52] kernels $k(\boldsymbol{x}, \boldsymbol{x}')$ permit the regression of continuous functions up to arbitrarily high precision [38]. Also, we allow Gaussian measurement noise without any boundedness assumptions as in, e.g., [28], [30], [39].

The functional probability distribution defined by the multidimensional GP in Assumption 1 is now explicitly leveraged to bound the model error, thus leading us to one of the main contributions of this article. At first, we consider the unknown vector-valued function $\boldsymbol{f}\colon \mathcal{X} \to \mathbb{R}^N$ on a finite set $|\mathcal{X}| < \infty$.

Lemma 1: Pick a $\delta \in (0,1)$ and set $\beta \in \mathbb{R}^+$ such that

$$\beta(\delta) = \sqrt{2\Gamma_{N/2}^{-1}\left(\frac{\delta\gamma(N/2)}{|\mathcal{X}|}\right)}, \tag{14}$$

where $\Gamma_{N/2}^{-1}(\cdot)$ denotes the inverse of (1b) with $n = \frac{N}{2}$. Then, for $\boldsymbol{f}\colon \mathcal{X} \to \mathbb{R}^N$ satisfying Assumption 1 and $\underline{\lambda}(\cdot)$ indicating the minimal eigenvalue, the probabilistic bound

$$\Pr\left\{\|\boldsymbol{f}(\boldsymbol{x}) - \boldsymbol{\mu}_{\boldsymbol{f}}(\boldsymbol{x})\| \leq \beta(\delta)\underline{\lambda}^{\frac{1}{2}}(\boldsymbol{\Sigma}_{\boldsymbol{f}}(\boldsymbol{x}))\right\} = 1 - \delta \tag{15}$$

holds exactly $\forall \boldsymbol{x} \in \mathcal{X}$ on a finite set $|\mathcal{X}| < \infty$.

Proof: The proof is given in Appendix A. ■

With this result, we have circumvented the inaccuracy of bounding the probability (15) from below by using (1b) along with an adequate coordinate transformation, cf. the proof in Appendix A. This exact computation leads to significantly tighter guarantees, as demonstrated in the following. Before, however, we extend the support of (15) from a finite $|\mathcal{X}| < \infty$ to a compact set $\mathcal{X} \subseteq \mathbb{R}^M$. Purely for analysis purposes, we consider a discretization $\mathcal{X}_d \subset \mathcal{X}$ as done in [28]. Also, similar to the scalar approach [38], the continuity of the multidimensional function space and the GP-related estimates are leveraged to bound the error for a general $\boldsymbol{x} \in \mathcal{X}$.

Lemma 2: Pick a violation probability $\delta \in (0,1)$, a discretization constant $d \in \mathbb{R}^+$, and set

$$\beta(\delta, d) = \sqrt{2\Gamma_{N/2}^{-1}\left(\frac{\delta\gamma(N/2)}{M_d(\mathcal{X})}\right)} \tag{16}$$

with the covering number $M_d(\mathcal{X})$. Then, for $\boldsymbol{f}\colon \mathcal{X} \to \mathbb{R}^N$ satisfying Assumption 1, and compact $\mathcal{X} \subseteq \mathbb{R}^M$,

$$\Pr\left\{\|\boldsymbol{f}(\boldsymbol{x}) - \boldsymbol{\mu}_{\boldsymbol{f}}(\boldsymbol{x})\| \leq \beta(\delta, d)\sqrt{\underline{\lambda}(\boldsymbol{\Sigma}_{\boldsymbol{f}}(\boldsymbol{x})) + s(d)} + L_{\text{tot}}d\right\} = 1 - \delta \tag{17}$$

holds exactly $\forall \boldsymbol{x} \in \mathcal{X}$. Here, $s(d)$ is the modulus of continuity

$$s(d) = 2dL_{\boldsymbol{K}}\left(1 + D\|\boldsymbol{K}_{\boldsymbol{y}}^{-1}\|_F \max_{\boldsymbol{x},\boldsymbol{x}' \in \mathcal{X}} \|K(\boldsymbol{x}, \boldsymbol{x}')\|_F\right) \tag{18}$$

of the covariance $\boldsymbol{\Sigma}_{\boldsymbol{f}}$, where $\boldsymbol{K}_{\boldsymbol{y}} = \boldsymbol{K}(\boldsymbol{X}, \boldsymbol{X}) + \boldsymbol{\Sigma}_{\boldsymbol{\epsilon}}$, and

$$\|\boldsymbol{K}(\boldsymbol{x}, \cdot) - \boldsymbol{K}(\boldsymbol{x}', \cdot)\|_F \leq L_{\boldsymbol{K}}\|\boldsymbol{x} - \boldsymbol{x}'\|, \tag{19}$$

along with the Lipschitz constants of the function $L_{\boldsymbol{f}}$, the posterior mean $L_{\boldsymbol{\mu}} = L_{\boldsymbol{K}}\sqrt{D}\|\boldsymbol{K}_{\boldsymbol{y}}^{-1}\Delta\boldsymbol{y}\|$, where $\Delta\boldsymbol{y} = \text{vec}(\boldsymbol{Y} - \boldsymbol{m}(\boldsymbol{X}))$, and their sum $L_{\text{tot}} = L_{\boldsymbol{f}} + L_{\boldsymbol{\mu}}$.

Proof: See Appendix B. ■

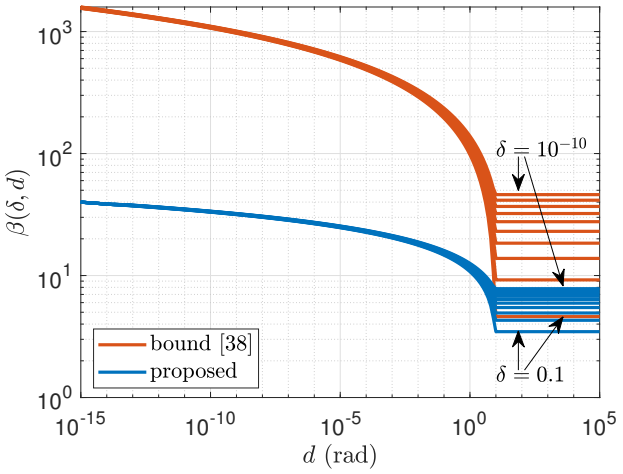

Fig. 1: Comparison of the proposed (blue) and approximative (red) bounds of Lemma 2 and [38], respectively, via their scaling factors $\beta(\delta, d)$, shown over the discretization d, for different probabilities $1 - \delta$ with $\delta = 10^{-x}$, $x = 1, 2, \ldots, 10$. Here, the $3N$-dimensional unit hyperball $\mathcal{X} = \{\boldsymbol{x} \in \mathbb{R}^{3N} \mid \|\boldsymbol{x}\| \leq 1\}$ with $N = 7$ is used as the supporting set.

The covering number $M_d(\mathcal{X})$ introduced in Lemma 2 is the cardinality of a finite discretization $|\mathcal{X}_d| < \infty$, needed to d-cover $\mathcal{X} \subseteq \mathbb{R}^M$ such that, for any $\boldsymbol{x} \in \mathcal{X}$, there exists $\boldsymbol{x}' \in \mathcal{X}_d$ with $\|\boldsymbol{x} - \boldsymbol{x}'\| \leq d$. For $c = \max_{\boldsymbol{x} \in \mathcal{X}}\|\boldsymbol{x}\|$, it can be bounded for $0 < d \leq 2c\sqrt{M}$ according to [53]

$$M_d(\mathcal{X}) \leq \left(\frac{2c\sqrt{M}}{d}\right)^M.$$

The Lipschitz constant $L_{\boldsymbol{f}}$ can be estimated analytically for Lagrangian systems, as shown in Appendix D. A probabilistic estimation based on Assumption 1 is also possible for general $\boldsymbol{f}(\boldsymbol{x})$, as demonstrated in [38] for the scalar case. The matrix kernel $L_{\boldsymbol{K}}$ can easily be estimated numerically, or even analytically by exploiting, if available, a kernel structure such as (6) and (11). Finally, given a set of observations, the last remaining Lipschitz constant $L_{\boldsymbol{\mu}}$ of the posterior mean directly follows from $L_{\boldsymbol{K}}$.

However, as can be seen by the bias term $(L_{\boldsymbol{f}} + L_{\boldsymbol{\mu}})d$ in the bound (17), the discretization in Lemma 2 introduces a constant approximation error. Therefore, it is desirable to let the grid constant d tend to zero to reduce the bias and, moreover, the impact of the unknown function's Lipschitz constant, which can only be bounded from above. The visualization in Fig. 1 demonstrates the efficacy of our bound compared with [38]. Despite small magnitudes of the grid constant d, the scaling factor $\beta(\delta, d)$ from (16) remains in a feasible region and is already significantly lower. Note that our proposed scale always remains well beneath [38], separated by a factor of up to 40. Although practically less relevant, this also holds for larger discretization constants, and all the way up to the maximal $d = 2\sqrt{21} \approx 9.17$ corresponding to a single discretization grid point. Since $\beta(\delta, d)$ is independent of the training data and the hyperparameters, Fig. 1 clearly indicates the theoretical superiority of the proposed bounds. These bounds are tightened even further in contrast to [30], which is restricted to uncorrelated and independent scalar functions for each dimension, by our leveraging of the joint functional distribution, leading to a dependence of (15) and (17) on the square root of the smallest eigenvalue of the covariance instead of the maximum (or all separate) standard deviation(s). Note that the latter are inherently larger, especially in regions outside the training domain, since correlations are neglected.

Remark 2: Contrary to [28], [30], [38], [39], probabilities are computed exactly in closed form up to dependence on gamma functions (1). The closed-form derivation of exact probabilities instead of their bounding from below [28], [38] keeps the resulting error bound significantly less conservative, even for $d \to 0$ and thus $|\mathcal{X}_d| \to \infty$ such that the discretization $\mathcal{X}_d$ desirably converges to the compact set $\mathcal{X}$. Note that a variety of different software tools, e.g., Python's SciPy or Matlab, are readily available for the numerical evaluation of the gamma functions and their inverses in Lemmas 1–2, as opposed to the bounds proposed in [28], [39], which depend on hardly computable constants such as the maximum information gain.

IV. Disturbance observation with L-GPs

In this section, we now leverage the uncertainty quantification of the model and its error bound in the design and stability analysis of our proposed data-driven and physically consistent disturbance observers. The following observer gains are proposed based on the posterior L-GP covariance $\boldsymbol{\Sigma}_{\boldsymbol{\tau}}(\boldsymbol{x})$ with kernel matrix $\boldsymbol{K}_{\boldsymbol{\tau}} = \mathcal{L}_{\boldsymbol{q}} \mathcal{L}_{\boldsymbol{q}'}^{\top} k_L + \boldsymbol{K}_f$ from (10).

Lemma 3: The uncertainty-adaptive gain

$$\boldsymbol{K}_O(\boldsymbol{\Sigma}_{\boldsymbol{\tau}}(\boldsymbol{x})) = \boldsymbol{K}_3(\boldsymbol{K}_2 + \boldsymbol{\Sigma}_{\boldsymbol{\tau}}(\boldsymbol{x}))^{-1}\boldsymbol{K}_3 + \boldsymbol{K}_1 \tag{20}$$

with constant $\mathbf{0} \prec \underline{k}_i \boldsymbol{I} \prec \boldsymbol{K}_i \prec \bar{k}_i \boldsymbol{I}$, where $\underline{k}_i, \bar{k}_i \in \mathbb{R}^+$ for $i = 1, 2, 3$, is always guaranteed to fulfill the bounds

$$\underline{k}_1 \boldsymbol{I} \prec \boldsymbol{K}_O(\boldsymbol{\Sigma}_{\boldsymbol{\tau}}(\boldsymbol{x})) \prec \left(\frac{\bar{k}_3^2}{\underline{k}_2} + \bar{k}_1\right) \boldsymbol{I}\,. \tag{21}$$

Proof: Directly follows from Weyl's inequality [54, III.2.1] for the eigenvalues of the sum of symmetric matrices and Lidskii's corollary [54, III.4.6] for the eigenvalues of the product of positive definite matrices. ■

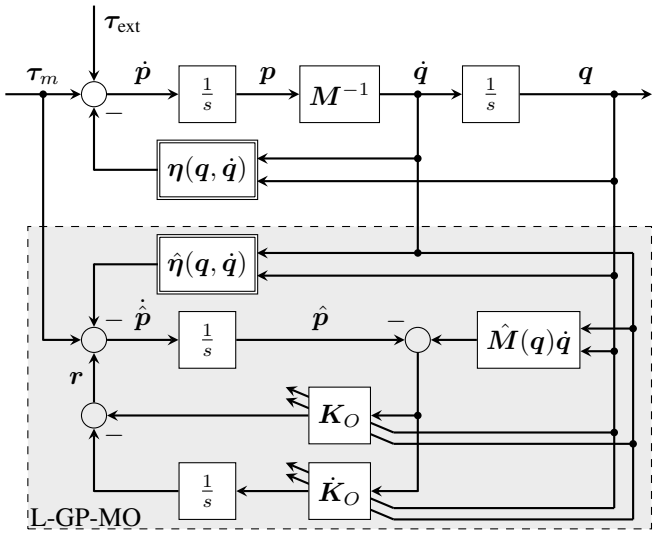

Fig. 2: Block diagram of the L-GP-based momentum observer (23b) for $\dot{\boldsymbol{p}}$ with virtual measurement $\boldsymbol{p} = \hat{\boldsymbol{M}}(\boldsymbol{q})\dot{\boldsymbol{q}}$.

Remark 3: Assuming perfect model knowledge, the MO can be shown to converge to a virtual sensor for disturbances with increasing correction gain [11]. Thus, contrary to the scalar GP-based, adaptive control law [30], we follow the inverse goal of decreasing the gain in areas where model confidence is low and vice versa. The uncertainty-adaptive gain $\boldsymbol{K}_O$ always remains between user-definable lower and upper bounds (21). Different covariance-based adaptations are also possible, for example, with integrated covariance over time.

The next theorem introduces our proposed observer structure, depicted in Fig. 2, for estimating external disturbances acting on joint level. For compactness, we define [11]

$$\begin{aligned}\boldsymbol{\eta}(\boldsymbol{q}, \dot{\boldsymbol{q}}) &\coloneqq \boldsymbol{g}(\boldsymbol{q}) + \boldsymbol{C}(\boldsymbol{q}, \dot{\boldsymbol{q}})\dot{\boldsymbol{q}} - \dot{\boldsymbol{M}}(\boldsymbol{q})\dot{\boldsymbol{q}} + \boldsymbol{\tau}_f(\boldsymbol{q}, \dot{\boldsymbol{q}}) \\ &= \boldsymbol{g}(\boldsymbol{q}) - \boldsymbol{C}^T(\boldsymbol{q}, \dot{\boldsymbol{q}})\dot{\boldsymbol{q}} + \boldsymbol{\tau}_f(\boldsymbol{q}, \dot{\boldsymbol{q}})\,.\end{aligned} \tag{22}$$

We are now ready to formulate the first main result.

Theorem 1 (L-GP-MO): Consider for $\boldsymbol{p} = \hat{\boldsymbol{M}}(\boldsymbol{q})\dot{\boldsymbol{q}}$ the L-GP-based momentum observer given by

$$\dot{\hat{\boldsymbol{p}}} = \boldsymbol{\tau}_m - \hat{\boldsymbol{\eta}}(\boldsymbol{q}, \dot{\boldsymbol{q}}) + \boldsymbol{r} \tag{23a}$$

$$\dot{\boldsymbol{r}} = \boldsymbol{K}_O(\boldsymbol{\Sigma}_{\boldsymbol{\tau}})(\dot{\boldsymbol{p}} - \dot{\hat{\boldsymbol{p}}}) \tag{23b}$$

with L-GP means $\hat{\boldsymbol{M}}(\boldsymbol{q})$, $\hat{\boldsymbol{\eta}}(\boldsymbol{q}, \dot{\boldsymbol{q}})$, and covariance-based $\boldsymbol{K}_O(\boldsymbol{\Sigma}_{\boldsymbol{\tau}})$ according to (20). Then, for constant $\dot{\boldsymbol{\tau}}_{\text{ext}} = \mathbf{0}$ and any initial $\boldsymbol{e}_0 \in \mathbb{R}^N$, $t_0 \in \mathbb{R}$, the observation error $\boldsymbol{e} = \boldsymbol{r} - \boldsymbol{\tau}_{\text{ext}}$ converges exponentially to a ball with probability

$$\Pr\left\{\|\boldsymbol{e}(t)\| \leq \varrho(\Delta) + c(\boldsymbol{e}_0)e^{-\alpha(t-t_0)}\right\} = 1 - \delta \tag{24}$$

and violation probability $\delta \in (0, 1)$, radius $\varrho(\Delta) = \Delta\bar{k}/\underline{k}$ with error bound $\Delta \in \mathbb{R}^+$, convergence rate $\alpha = \underline{k}/2$, eigenvalue bounds $\underline{k} \coloneqq \underline{k}_1$ and $\bar{k} \coloneqq \bar{k}_3^2/\underline{k}_2 + \bar{k}_1$ from (21), and scale

$$c(\boldsymbol{e}_0) = \begin{cases} 0\,, & \|\boldsymbol{e}_0\| \leq \varrho \\ \sqrt{\|\boldsymbol{e}_0\|^2 - \varrho^2(\Delta)}\,, & \|\boldsymbol{e}_0\| > \varrho \end{cases}. \tag{25}$$

Proof: For the proof of Theorem 1, we utilize a standard Lyapunov function and bound its derivative along the trajectories of the error dynamics of (23) from above, using the model error bound derived in Lemma 2, and the exponential stability theorem from [55]. To begin with, we reformulate (23b) by differentiating $\dot{\boldsymbol{p}} = \hat{\boldsymbol{M}}\dot{\boldsymbol{q}} + \hat{\boldsymbol{M}}\ddot{\boldsymbol{q}}$ and using (2) such that

$$\dot{\boldsymbol{r}} = \boldsymbol{K}_O(\boldsymbol{\Sigma}_{\boldsymbol{\tau}})(\hat{\boldsymbol{\tau}}(\boldsymbol{q},\dot{\boldsymbol{q}},\ddot{\boldsymbol{q}}) - \boldsymbol{\tau}_m - \boldsymbol{r})\,. \tag{26}$$

Plugging $\boldsymbol{\tau}_m = \boldsymbol{\tau} - \boldsymbol{\tau}_{\text{ext}}$ from (2) into (26) and introducing the model error $\tilde{\boldsymbol{\tau}} = \boldsymbol{\tau} - \hat{\boldsymbol{\tau}}$, we obtain the error dynamics

$$\dot{\boldsymbol{e}} + \boldsymbol{K}_O(\boldsymbol{\Sigma}_{\boldsymbol{\tau}})(\boldsymbol{e} + \tilde{\boldsymbol{\tau}}) = \boldsymbol{0}\,, \tag{27}$$

for $\dot{\boldsymbol{\tau}}_{\text{ext}} = \boldsymbol{0}$. Next, we consider the standard unweighted, time-invariant Lyapunov energy function

$$V(\boldsymbol{e}) = \tfrac{1}{2}\boldsymbol{e}^\top\boldsymbol{e} \tag{28}$$

and compute its time derivative along trajectories of (27) as

$$\dot{V} = -\boldsymbol{e}^\top\boldsymbol{K}_O(\boldsymbol{\Sigma}_{\boldsymbol{\tau}})(\boldsymbol{e} + \tilde{\boldsymbol{\tau}})\,.$$

Then, using the eigenvalues (21) from Lemma 3, we obtain

$$\dot{V} \leq -\underbrace{\underline{k}_1}_{=\underline{k}}\|\boldsymbol{e}\|^2 + \underbrace{\left(\tfrac{\bar{k}_3^2}{\underline{k}_2} + \bar{k}_1\right)}_{=\bar{k}}\|\tilde{\boldsymbol{\tau}}\|\|\boldsymbol{e}\|\,.$$

Exploiting Young's inequality in the form of $ab \leq \frac{a^2}{2\epsilon} + \frac{\epsilon b^2}{2}$ for nonnegative $a, b \geq 0$ and positive $\epsilon \in \mathbb{R}^+$, we bound the second term which is linear in $\|\boldsymbol{e}\|$ and get

$$\dot{V} \leq -2\left(\underline{k} - \tfrac{\epsilon}{2}\bar{k}^2\right)\tfrac{1}{2}\|\boldsymbol{e}\|^2 + \tfrac{\|\tilde{\boldsymbol{\tau}}\|^2}{2\epsilon} \leq -2\alpha(\epsilon)V + \tfrac{\|\tilde{\boldsymbol{\tau}}\|^2}{2\epsilon}$$

with convergence rate $\alpha(\epsilon) = \underline{k} - \frac{\epsilon}{2}\bar{k}^2$. Finally, we apply Lemma 2 and arrive at the probability

$$\Pr\left\{\dot{V} \leq -2\alpha(\epsilon)\left(V - \tfrac{\varrho^2(\epsilon)}{2}\right)\right\} = 1 - \delta$$

guaranteeing uniform ultimate boundedness and exponential convergence [55] to the closed ball

$$B(\Delta) = \left\{\boldsymbol{e} \in \mathbb{R}^N \middle| \|\boldsymbol{e}(t)\| \leq \varrho(\Delta)\,, \forall t \geq t_0\right\} \tag{29}$$

with radius

$$\varrho(\Delta) = \tfrac{\Delta}{\sqrt{2\epsilon\alpha(\epsilon)}} = \tfrac{\Delta}{\sqrt{\epsilon(2\underline{k} - \epsilon\bar{k}^2)}}\,. \tag{30}$$

The dynamics (27) are also exponentially stable to within $B(\Delta)$ with the same probability. Here, we have used $\forall \boldsymbol{x} \in \mathcal{S}$ the model error bound $\Delta \in \mathbb{R}^+$ such that

$$\mathcal{S} = \{\beta(\delta, d)\sqrt{\underline{\lambda}(\boldsymbol{\Sigma}_{\boldsymbol{\tau}}(\boldsymbol{x})) + s(d)} + (L_{\boldsymbol{\tau}} + L_{\boldsymbol{\mu}_{\boldsymbol{\tau}}})d \leq \Delta\}\,. \tag{31}$$

Optimizing (30) by minimization over ϵ, we set $\epsilon = \underline{k}/\bar{k}^2$, leading to the radius $\varrho(\Delta) = \Delta\bar{k}/\underline{k}$ of the ball (29) and the convergence rate $\alpha = \underline{k}/2$. ■

Theorem 1 presents, for a high probability $1 - \delta$, a uniform ultimate bound for the error dynamics (27) of the observer (23), proven to be exponentially stable with provided convergence rate α. In contrast to [11], uncertainties in the mass-inertia matrix and momentum are explicitly accounted for. The radius ϱ of the ball (29) depends linearly on an upper bound on the model error (31). Therefore, ϱ decreases with the minimal eigenvalue of the L-GP posterior covariance $\boldsymbol{\Sigma}_{\boldsymbol{\tau}}$. Note that, from (29), it might seem optimal to enforce an identical and constant correction via $\bar{k} = \underline{k}$ and let $\bar{k} \to \infty$. However, the performance of such a high-gain observer, essentially an approximate differentiator, is practically limited by measurement noise and uncertain dynamics [56]. Thus, let us consider the instantaneous model error bound $\Delta(t)$ by allowing the set $\mathcal{S}$ to include only the current state $\boldsymbol{x}(t)$, thus leading to a direct scaling of the radius $\varrho(t)$ by the bound in Lemma 2. Then, extending the upper eigenvalue bound of the gain (21) to $\bar{k}(t) = \bar{k}_3^2(\underline{k}_2 + \underline{\lambda}(\boldsymbol{\Sigma}_{\boldsymbol{\tau}}))^{-1} + \bar{k}_1$ with $\underline{k} = \underline{k}_1$, it becomes clear that the finite adaptation (20) is advantageous since it compensates an increase of the radius (29) through the model error bound, which is scaled by $\underline{\lambda}(\boldsymbol{\Sigma}_{\boldsymbol{\tau}})$.

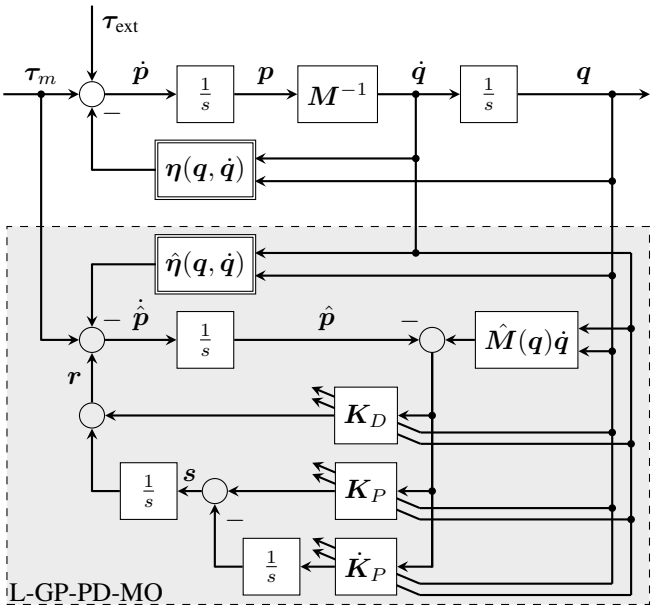

Fig. 3: Block diagram of the L-GP-based PD momentum observer (34) for $\dot{\boldsymbol{p}}$ with uncertainty-adaptive P-feedback and virtual measurement $\boldsymbol{p} = \hat{\boldsymbol{M}}(\boldsymbol{q})\dot{\boldsymbol{q}}$.

Moreover, note that the observer output signal $\boldsymbol{r}(t)$, also called residual vector, follows from integration by parts of (23b), resulting in

$$\boldsymbol{r} = \boldsymbol{K}_O\left(\boldsymbol{p} - \hat{\boldsymbol{p}}\right) - \int_{t_0}^{t}\dot{\boldsymbol{K}}_O\left(\boldsymbol{p} - \hat{\boldsymbol{p}}\right)d\tau \tag{32}$$

with

$$\hat{\boldsymbol{p}}(t) = \boldsymbol{p}(0) + \int_{t_0}^{t}\left(\boldsymbol{\tau}_m - \hat{\boldsymbol{\eta}}(\boldsymbol{q},\dot{\boldsymbol{q}}) + \boldsymbol{r}\right)d\tau\,. \tag{33}$$

Also, note that the MO (23) enables estimating the accelerations $\ddot{\boldsymbol{q}}$ via $\hat{\ddot{\boldsymbol{q}}} = \hat{\boldsymbol{M}}^{-1}(\boldsymbol{\tau}_m + \boldsymbol{r} - \hat{\boldsymbol{n}})$, where $\hat{\boldsymbol{n}} = \hat{\boldsymbol{C}}\dot{\boldsymbol{q}} + \hat{\boldsymbol{g}} + \hat{\boldsymbol{\tau}}_f$. Next, we introduce a PD observer structure based on [57].

Theorem 2 (L-GP-PD-MO): Consider for $\boldsymbol{p} = \hat{\boldsymbol{M}}(\boldsymbol{q})\dot{\boldsymbol{q}}$ the L-GP-based PD momentum observer given by

$$\dot{\hat{\boldsymbol{p}}} = \boldsymbol{\tau}_m - \hat{\boldsymbol{\eta}}(\boldsymbol{q},\dot{\boldsymbol{q}}) + \boldsymbol{r} \tag{34a}$$

$$\dot{\boldsymbol{s}} = \boldsymbol{K}_P(\boldsymbol{\Sigma}_{\boldsymbol{\tau}})(\dot{\boldsymbol{p}} - \dot{\hat{\boldsymbol{p}}}) \tag{34b}$$

$$\dot{\boldsymbol{r}} = \boldsymbol{s} + \boldsymbol{K}_D(\dot{\boldsymbol{p}} - \dot{\hat{\boldsymbol{p}}}) \tag{34c}$$

with L-GP mean estimates $\hat{\boldsymbol{M}}(\boldsymbol{q})$ and $\hat{\boldsymbol{\eta}}(\boldsymbol{q},\dot{\boldsymbol{q}})$, constant derivative gain $\boldsymbol{K}_D \succ \boldsymbol{I}$, and covariance-based $\boldsymbol{K}_P(\boldsymbol{\Sigma}_{\boldsymbol{\tau}})$ according to (20). Then, for constant velocity disturbances $\ddot{\boldsymbol{\tau}}_{\text{ext}} = \boldsymbol{0}$ and any initial conditions $\boldsymbol{e}_0, \dot{\boldsymbol{e}}_0 \in \mathbb{R}^N$, $t_0 \in \mathbb{R}$, the estimation error $\boldsymbol{e} = \boldsymbol{r} - \boldsymbol{\tau}_{\text{ext}}$ vanishes exponentially with probability

$$\Pr\left\{\|[\boldsymbol{e}(t), \dot{\boldsymbol{e}}(t)]\| \leq \varrho(\Delta, \tilde{\Delta}) + c(\boldsymbol{e}_0, \dot{\boldsymbol{e}}_0) e^{-\alpha(t-t_0)}\right\} \geq 1 - \delta$$

for $\delta \in (0,1)$ with model error and derivative bounds $\Delta, \tilde{\Delta} \in \mathbb{R}^+$ and scale $c(\cdot)$ analogously to (25). Radius $\varrho(\Delta, \tilde{\Delta})$ and exponential rate of convergence $\alpha(\epsilon, \varphi)$ are given by

$$\varrho(\Delta, \tilde{\Delta}) = \sqrt{\frac{\left(\frac{\epsilon}{\varphi} + \frac{1}{\vartheta + \epsilon\varphi}\right)\bar{k}_P \Delta^2 + \left(\frac{\epsilon}{\varphi} + \frac{1}{\epsilon(\vartheta+\varphi)}\right)\bar{k}_D \tilde{\Delta}^2}{2(1-\epsilon)\alpha(\epsilon,\varphi)}} \tag{35a}$$

$$\alpha(\epsilon, \varphi) = \frac{1}{1+\epsilon}\left(\underline{k}_D - \epsilon - \frac{1}{2\vartheta} - \epsilon\frac{\vartheta+\varphi}{2}\bar{k}_D - \frac{\vartheta+\epsilon\varphi}{2}\bar{k}_P\right) \tag{35b}$$

and specified by $\epsilon, \varphi \in \mathbb{R}^+$ and fixed $\vartheta \in \mathbb{R}^+$ satisfying

$$0 < \epsilon < \min\left(1,\ \frac{\underline{k}_D - 1}{\underline{k}_P + 1},\ \frac{2\underline{k}_D - \frac{1}{\vartheta} - \vartheta\bar{k}_P}{1 + \vartheta\bar{k}_D + \varphi(\bar{k}_P + \bar{k}_D)}\right), \tag{36a}$$

$$\vartheta = \underline{k}_D - \epsilon(\underline{k}_P + 1) \pm \sqrt{\left[\underline{k}_D - \epsilon\left(\underline{k}_P + 1\right)\right]^2 - 1}\,. \tag{36b}$$

Here, $\underline{k}_P = \underline{\lambda}(\boldsymbol{K}_P)$ and $\bar{k}_P = \bar{\lambda}(\boldsymbol{K}_P)$ denote the minimal and maximal eigenvalues of $\boldsymbol{K}_P$, respectively, bounded by (21).

Proof: Firstly, we differentiate the last line of (34) and get

$$\ddot{\boldsymbol{r}} = -\boldsymbol{K}_P(\boldsymbol{\Sigma}_{\boldsymbol{\tau}})(\boldsymbol{r} - \boldsymbol{\tau}_{\text{ext}} + \tilde{\boldsymbol{\tau}}) - \boldsymbol{K}_D(\dot{\boldsymbol{r}} - \dot{\boldsymbol{\tau}}_{\text{ext}} + \dot{\tilde{\boldsymbol{\tau}}})\,,$$

where we have again used $\dot{\boldsymbol{p}} - \dot{\hat{\boldsymbol{p}}} = -\tilde{\boldsymbol{\tau}} + \dot{\boldsymbol{\tau}}_{\text{ext}} - \boldsymbol{r}$ analogously to the derivation of (26). The error dynamics of (34) then follow from $\boldsymbol{e} = \boldsymbol{r} - \boldsymbol{\tau}_{\text{ext}}$ and $\ddot{\boldsymbol{e}} = \ddot{\boldsymbol{r}}$ according to

$$\ddot{\boldsymbol{e}} + \boldsymbol{K}_D(\dot{\boldsymbol{e}} + \dot{\tilde{\boldsymbol{\tau}}}) + \boldsymbol{K}_P(\boldsymbol{\Sigma}_{\boldsymbol{\tau}})(\boldsymbol{e} + \tilde{\boldsymbol{\tau}}) = \boldsymbol{0} \tag{37}$$

with model error $\tilde{\boldsymbol{\tau}} = \boldsymbol{\tau} - \hat{\boldsymbol{\tau}}$. Next, we consider the following time-invariant Lyapunov energy function

$$V(\boldsymbol{e}, \dot{\boldsymbol{e}}) = \tfrac{1}{2}\left(\|\boldsymbol{e}\|^2 + \|\dot{\boldsymbol{e}}\|^2\right) + \epsilon\boldsymbol{e}^\top\dot{\boldsymbol{e}} \tag{38}$$

with positive $0 < \epsilon < 1$. Thus, using Young's inequality in the form of $ab \leq \frac{a^2}{2\varphi} + \frac{\varphi b^2}{2}$ for nonnegative $a, b \geq 0$, we can derive that (38) is bounded $\forall \boldsymbol{e}, \dot{\boldsymbol{e}} \in \mathbb{R}^N$ by

$$\tfrac{1-\epsilon}{2}(\|\boldsymbol{e}\|^2 + \|\dot{\boldsymbol{e}}\|^2) \leq V \leq \tfrac{1+\epsilon}{2}(\|\boldsymbol{e}\|^2 + \|\dot{\boldsymbol{e}}\|^2)\,.$$

Next, we differentiate (38) w.r.t. time t, leading to

$$\begin{aligned}\dot{V} &= \boldsymbol{e}^\top\dot{\boldsymbol{e}} + \dot{\boldsymbol{e}}^\top\ddot{\boldsymbol{e}} + \epsilon(\|\dot{\boldsymbol{e}}\|^2 + \boldsymbol{e}^\top\ddot{\boldsymbol{e}}) \\ &= -\epsilon\boldsymbol{e}^\top\boldsymbol{K}_P\boldsymbol{e} - \dot{\boldsymbol{e}}^\top(\boldsymbol{K}_D - \epsilon\boldsymbol{I})\dot{\boldsymbol{e}} \\ &\quad -\boldsymbol{e}^\top\left(\boldsymbol{K}_P + \epsilon\boldsymbol{K}_D - \boldsymbol{I}\right)\dot{\boldsymbol{e}} - (\epsilon\boldsymbol{e} + \dot{\boldsymbol{e}})^\top(\boldsymbol{K}_D\dot{\tilde{\boldsymbol{\tau}}} + \boldsymbol{K}_P\tilde{\boldsymbol{\tau}})\,.\end{aligned}$$

Then, making use of the Cauchy-Schwarz and Weyl's [54, III.2.1] inequalities, we upper bound $\dot{V}$ by

$$\begin{aligned}\dot{V} \leq &-\epsilon\underline{k}_P\|\boldsymbol{e}\|^2 - (\underline{k}_D - \epsilon)\|\dot{\boldsymbol{e}}\|^2 + (\bar{k}_P + \epsilon\bar{k}_D - 1)\|\boldsymbol{e}\|\|\dot{\boldsymbol{e}}\| \\ &+ (\epsilon\|\boldsymbol{e}\| + \|\dot{\boldsymbol{e}}\|)\left(\bar{k}_P\|\tilde{\boldsymbol{\tau}}\| + \bar{k}_D\|\dot{\tilde{\boldsymbol{\tau}}}\|\right)\,.\end{aligned}$$

Again, exploiting Young's inequality, we follow that

$$\begin{aligned}\dot{V} \leq &-(\underline{k}_D - \epsilon - \tfrac{1}{2\vartheta} - \epsilon\tfrac{\vartheta+\varphi}{2}\bar{k}_D - \tfrac{\vartheta+\epsilon\varphi}{2}\bar{k}_P)(\|\boldsymbol{e}\|^2 + \|\dot{\boldsymbol{e}}\|^2) \\ &+ (\tfrac{\epsilon}{\varphi} + \tfrac{1}{\vartheta+\epsilon\varphi})\tfrac{\bar{k}_P\|\tilde{\boldsymbol{\tau}}\|^2}{2} + (\tfrac{\epsilon}{\varphi} + \tfrac{1}{\epsilon(\vartheta+\varphi)})\tfrac{\bar{k}_D\|\dot{\tilde{\boldsymbol{\tau}}}\|^2}{2}\,,\end{aligned}$$

having newly introduced the parameter $\varphi \in \mathbb{R}^+$ and the fixed constant ϑ given by (36b), requiring additionally that $\epsilon \leq \frac{\underline{k}_D - 1}{\underline{k}_P + 1}$ such that $\vartheta \in \mathbb{R}^+$. Finally, we apply Lemma 2 along with its derivative extension in Appendix C to get

$$\Pr\left\{\dot{V} \leq -2\alpha(\epsilon,\varphi)\left(V - \tfrac{1-\epsilon}{2}\varrho^2(\Delta, \tilde{\Delta})\right)\right\} \geq 1 - 2\delta \tag{39}$$

with radius ϱ and convergence rate α from (35a) and (35b), respectively [55]. Here, we have leveraged De Morgan's law and the union bound $\forall(\boldsymbol{x}, \dot{\boldsymbol{x}}) \in \mathcal{S}$ such that

$$\mathcal{S} = \left\{\beta(\delta, d)l(\boldsymbol{x}, d) \leq \Delta \ \cap\ \beta(\delta, d)\tilde{l}(\boldsymbol{x}, d)\|\dot{\boldsymbol{x}}\| \leq \tilde{\Delta}\right\} \tag{40}$$

with $l(\boldsymbol{x}, d) = \sqrt{\bar{\lambda}(\boldsymbol{\Sigma}_{\boldsymbol{\tau}}(\boldsymbol{x})) + s(d)} + (L_{\boldsymbol{\tau}} + L_{\boldsymbol{\mu}})d$ and $\tilde{l}(\cdot)$ defined analogously for $\text{vec}(\frac{\partial \boldsymbol{\tau}}{\partial \boldsymbol{x}})$. Lastly, setting $\tilde{\delta} = 2\delta$ in (39), we finish the proof. ∎

Theorem 2 extends the observer (23) by a derivative correction, leading to the structure (34), and also provides for a high probability $1 - \delta$ a uniform ultimate bound for its exponentially stable, second-order error dynamics (37). The convergence rate (35b) and radius (35a) are now specified by parameters ϵ, φ from (36), permitting a larger measure of design freedom. Essentially, the observer outputs $\boldsymbol{s}(t), \boldsymbol{r}(t)$ follow from integration. To see this, we express the derivative output $\boldsymbol{s}$ by integration in parts of the second line of (34) as

$$\boldsymbol{s} = \boldsymbol{K}_P\left(\boldsymbol{p} - \hat{\boldsymbol{p}}\right) - \int_{t_0}^{t}\dot{\boldsymbol{K}}_P\left(\boldsymbol{p} - \hat{\boldsymbol{p}}\right)d\tau\,, \tag{41}$$

Here, $\hat{\boldsymbol{p}}$ is computed subsequently by integration

$$\hat{\boldsymbol{p}}(t) = \boldsymbol{p}(0) + \int_0^t\left(\boldsymbol{\tau}_m - \hat{\boldsymbol{\eta}}(\boldsymbol{q}, \dot{\boldsymbol{q}}) - \hat{\boldsymbol{\tau}}_f(\boldsymbol{q}, \dot{\boldsymbol{q}}) + \boldsymbol{r}\right)d\tau\,. \tag{42}$$

Finally, the output signal $\boldsymbol{r}$ then follows by integrating the last line of (34) and reformulating according to

$$\boldsymbol{r} = \int_{t_0}^{t}\boldsymbol{s}(\tau)d\tau + \boldsymbol{K}_D\left(\boldsymbol{p} - \hat{\boldsymbol{p}}\right) \tag{43}$$

with $\boldsymbol{s}$ and $\hat{\boldsymbol{p}}$ from (41) and (42), respectively.

Remark 4: The reduced MO (23) from Theorem 1 can be recovered from (34) of Theorem 2 by setting $\boldsymbol{K}_P = \boldsymbol{0}$ and $\boldsymbol{K}_D = \boldsymbol{K}_O$.

V. Experimental Evaluation

In this section, we illustrate the efficacy of our modeling approach in numerical simulation and demonstrate the performance and effectiveness of our proposed error bounds and L-GP-augmented momentum observers in a series of experiments on a 7-DOF KUKA IIWA [58]. Additionally, we compare with state-of-the-art linear-parametric modeling and identification schemes based on Least Squares (LS) [9], [23], [59], and with the standard black-box GP with squared exponential (SE) kernel [26], [27].

A. Numerical Simulations

To begin with, we validate the physical consistency of our model based on the two-link manipulator from [45, p. 164] with gravitation, as described in detail in [41]. Here, we have additionally included unit damping elements at each joint and extended the training data set to $D = 34$ noisy measurement

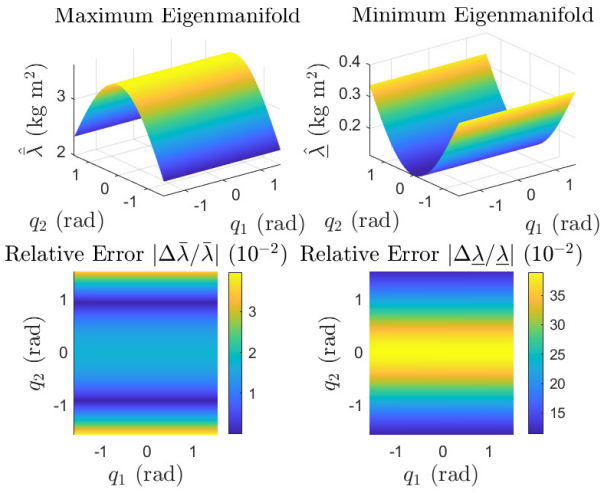

Fig. 4: L-GP estimate of the mass-inertia matrix for the two-link manipulator: eigenmanifolds for $\boldsymbol{q} \in [-\pi/2, \pi/2]^2$.

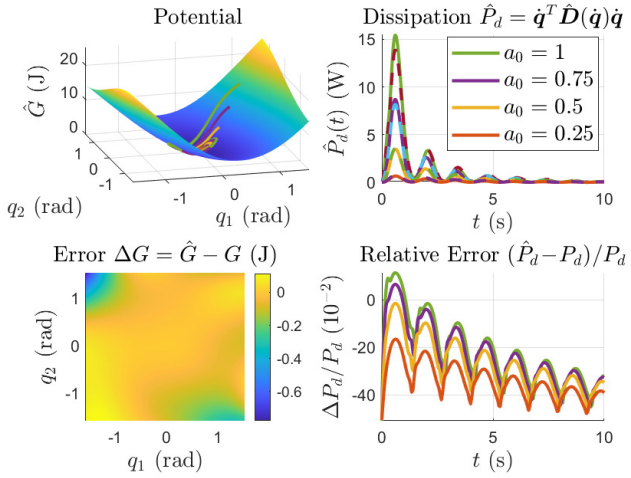

Fig. 5: L-GP gravity estimate for the two-link robotic manipulator and numerically simulated trajectories of the unforced estimative dynamics for different initial conditions $\boldsymbol{q}(0) = a_0\mathbf{1}$.

pairs by including an equidistant 3×3 grid for $\dot{\boldsymbol{q}}_i \in [-1, 1]^2$ with fixed $\boldsymbol{q}_i = \ddot{\boldsymbol{q}}_i = \mathbf{0}$.

The accurate approximation of the positive definite subfunctional kinetic energy space is shown in Fig. 4 w.r.t. the eigenvalues of the mass-inertia estimate, evaluated over the domain $\boldsymbol{q} \in [-\pi/2, \pi/2]^2$, which is significantly larger than the training domain $\boldsymbol{q}_i \in [-1, 1]^2$. Physical consistency in terms of positive semi-definiteness of the gravitational estimate is illustrated in Fig. 5, along with the passivity of the L-GP-based dynamics simulated for different initial conditions $\boldsymbol{q}(0) = a_0\mathbf{1}$, $\dot{\boldsymbol{q}}(0) = \mathbf{0}$.

Moving on to higher system complexity, we consider the planar soft robot from [9], [60] simulated by a FEM model. For this, we employ a discretization of a continuum rod as a series of infinitesimal links [61], where we consider a total of $N_{\text{FEM}} = 100$, subsequently connected by linear torsional-spring-damper elements, and thus equally dividing the continuous rod with unit mass and length. The stiffnesses and dampings are set to 10 Nm rad^{-1} and 1 Nm s rad^{-1}, respectively. For training, we consider the system's step response to a constant torque with amplitude $a = 1$ Nm acting on each FEM element, starting from equilibrium, i.e., the orientation aligned with gravity along the x-axis, cf. the dotted line in Fig. 6 (left), and measurement noise $\boldsymbol{\epsilon} \sim \mathcal{N}(\mathbf{0}, \sigma_\epsilon^2 \boldsymbol{I})$, $\sigma_\epsilon = 0.01a$. The L-GP uses $D = 24$ equidistant training data pairs and discretizes the system into $N = 4$ constant curvature (CC) segments, as done in the parametric model proposed in [9] equivalent to a constrained rigid body with $4N = 16$ DOFs. The evolution of the inertia matrix's eigenvalues, obtained by resimulating the L-GP-based dynamics for the same step input, is shown in Fig. 6 (right), whereas the resulting curvature angle trajectories are visualized in Fig. 7, respectively. As a comparison, we identified the inertial, damping, and stiffness parameters of the CC model proposed in [9] via Least Squares (LS), showing inferior modeling accuracy. The L-GP's performance is validated dynamically in Fig. 8 for various step inputs. The results show that trajectories can be predicted accurately despite the additional presence of discretization errors due to numerical integration.

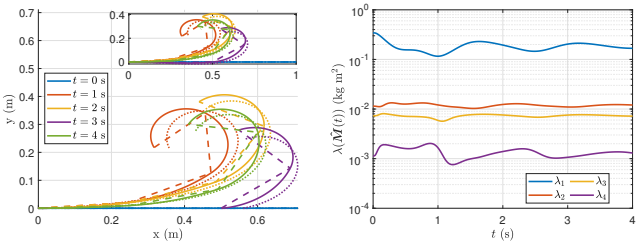

Fig. 6: Numerically simulated L-GP-based step response of the soft robot [9] for $a = 1$ Nm. Left: continuous orientations of L-GP (solid lines) and FEM (dotted) for different time instances. Right: inertia matrix eigenvalues of the equivalent L-GP-based system discretizing into $N = 4$ constant curvature segments.

B. Elastic Joint Robot: KUKA LBR IIWA 14 R820

In the remaining sections, we validate the proposed multidimensional error bound as well as the L-GP-based momentum observers directly in experiments, using a KUKA IIWA [58], a fully actuated, lightweight, elastic joint robot with 7 DOFs. Additionally, we compare our performance with KUKA's built-in external torque observer. Position and torque measurements are obtained from KUKA's Fast Robot Interface (FRI) sampled at 1 kHz. Velocities and accelerations are computed by successive differentiation and filtering.

For the L-GP, we use only $D = 100$ equidistant samples $\{\boldsymbol{q}_i, \dot{\boldsymbol{q}}_i, \ddot{\boldsymbol{q}}_i, \boldsymbol{\tau}_i\}$ of a 20 s excitation trajectory. We account for uncertainty in acceleration and torque measurements by setting noise covariances to $\boldsymbol{\Sigma}_{\boldsymbol{\tau}} = \sigma_\tau^2 \boldsymbol{I}$ and $\boldsymbol{\Sigma}_{\ddot{\boldsymbol{q}}} = \sigma_{\ddot{q}}^2 \boldsymbol{I}$ with variances $\sigma_\tau = 0.1$ Nm and $\sigma_{\ddot{q}} = 0.1$ rad s^{-2}, respectively, thus leading to standard deviations of $\sqrt{0.1} \approx 0.32$. A total of 45 hyperparameters are optimized based on the least-squares approximation of another set of $3D$ equidistant samples. All

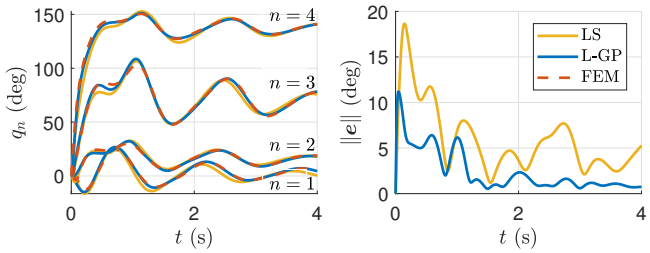

Fig. 7: Resimulated training trajectory of the models showing the bending angles of the CC segments for $a = 1$ Nm. RMS errors of L-GP and LS are 1.65 and 3.86 deg, respectively.

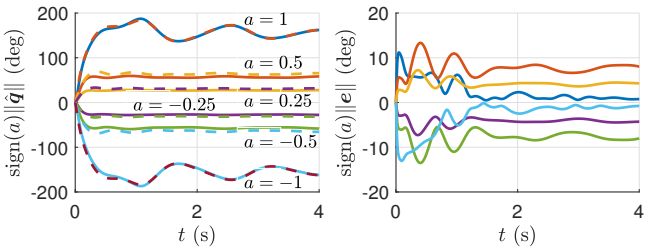

Fig. 8: Simulated validation trajectories of the L-GP-based dynamical model for different step inputs. Solid lines indicate the L-GP trajectories, dashed the FEM simulation.

hypervariances are identically initialized by ones, and the kinetic mass-inertia hypermetric, cf. [41], is reduced to a constant Euclidian form with identical length scale initialized by π. In addition to the L-GP, we model transmission nonlinearities in the motor to joint gearing of the IIWA [62] by compositely employing independently structured GPs with periodic kernels for joints 2-4.

As a benchmark, we compare with the physically consistent parameter identification method in [23] based on Linear Matrix Inequalities (LMIs), using the convex optimization solver MOSEK and a total of 50 base parameters. This identified model is passed to the L-GP and used as its prior mean $\boldsymbol{m}_{\boldsymbol{\tau}}$, where gravity is modeled identically. Also, comparing with a standard unstructured GP with squared exponential kernel [27], we validate the different models based on a validation trajectory, which is significantly distinct from the excitation trajectory, shown in Fig. 9. Error norms of both are plotted over time as well, along with the proposed probabilistic bound from Lemma 2 applied to standard GP and L-GP, as well as the standard bound from [30], [38], for violation probability $\delta = 10^{-10}$ and discretization constant $d = 10^{-15}$, cf. Tab. II. Note that the latter cannot be applied to the L-GP since [38] is constrained to scalar functions, and the extension [30] requires an uncorrelated functional distribution, i.e., the covariances must be diagonal. Our proposed bound, however, cannot only deal with functional correlations but also explicitly leverages these, leading to several orders of magnitude improvements for both GP models. The standard GP displays an inferior estimation accuracy paired with an overly confident uncertainty measure compared to the L-GP.

The estimated contributions of inertial, gravitational, and friction effects, along with the transmission nonlinearity component, are shown in Fig. 10. The efficiency of the investigated models w.r.t. prediction accuracy and computation timings are compared in Fig. 12. All computations were performed on a standard notebook in Matlab with 3.2 GHz CPU and 16 GB RAM. In particular, the standard GP shows a strong overtraining effect, leading to a limited validation accuracy, while the L-GP shows a high data efficiency. Furthermore, due to the high dimensionality of the system, the L-GP is computationally faster than the MEX-compiled reference implementation of the standard GP modeling approach until a cardinality of $D = 80$. For $D = 40, 100$, its average prediction timings and validation errors are $364, 722\,\mu$s and $2.50, 2.45$ Nm, respectively. Also, comparing with the C-implementation of the standard GP method from [30] promises a further computational performance increase achievable for the L-GP by moving to a more efficient platform than Matlab.

Disturbance	$\boldsymbol{\tau}_{\text{ext}} = \mathbf{0}$		$\boldsymbol{\tau}_{\text{ext}}(t)$	
Observer	STD (Nm)	RMS (Nm)	STD (Nm)	RMS (Nm)
KUKA	0.7785	0.8567	0.8986	1.0104
Parametric MO	0.6330	0.8062	0.7151	0.9109
Static L-GP-MO	0.5699	0.7624	0.6475	0.8753
Static L-GP-PD-MO	0.4879	0.6941	0.5575	0.7046
$\boldsymbol{\Sigma}$-adapt. L-GP-MO	0.4672	0.6525	0.5697	0.7810
$\boldsymbol{\Sigma}$-adapt. L-GP-PD-MO	0.4864	0.6783	0.5330	0.6878

TABLE I: Numerical evaluation of the disturbance estimation errors for each considered MO variant on the KUKA IIWA.

C. Disturbance observation on the KUKA IIWA

Two scenarios are considered to validate the disturbance observers experimentally on the IIWA: firstly, we use the trajectories of the undisturbed robot from Fig. 9. Since no external torques are disturbing the system in this case, the observers should converge to $\boldsymbol{\tau}_{\text{ext}} = \mathbf{0}$, assuming error-free models. Secondly, we perform new measurements mounting a Schunk gripper to the end-effector of the robot and treating its inertial forces as a time-variant disturbance $\boldsymbol{\tau}_{\text{ext}}(t)$ acting upon the system, cf. Fig. 11. As a reference for the actual disturbance, we use the difference between the rigid-body model estimates with and without gripper, identified via physically consistent Least Squares (PC-LS) with LMIs and validated in the previous subsection. The performances of KUKA's built-in, the classical parametric, and the proposed L-GP-based static- and uncertainty-adaptive-gain disturbance observers are evaluated numerically for both cases in Tab. I, showing the standard deviation averaged per dimension and the overall RMS error. Parameter values are given in Tab. II; in particular, we use identical gain matrices for both scenarios. Compared with KUKA's external torque observer provided by the FRI, we are able to achieve relative improvements of up to 66.61% and 68.60% in the free and disturbed scenarios, respectively, w.r.t. the error's averaged standard deviation.

The evaluations show that the L-GP-based modeling approach and the uncertainty-based adaptation each lead to subsequent performance increases relative to the parametric and static-gain observer variants, respectively. Note that the matrix gains $\boldsymbol{K}_{1-3}$ were chosen such that the resulting uncertainty-

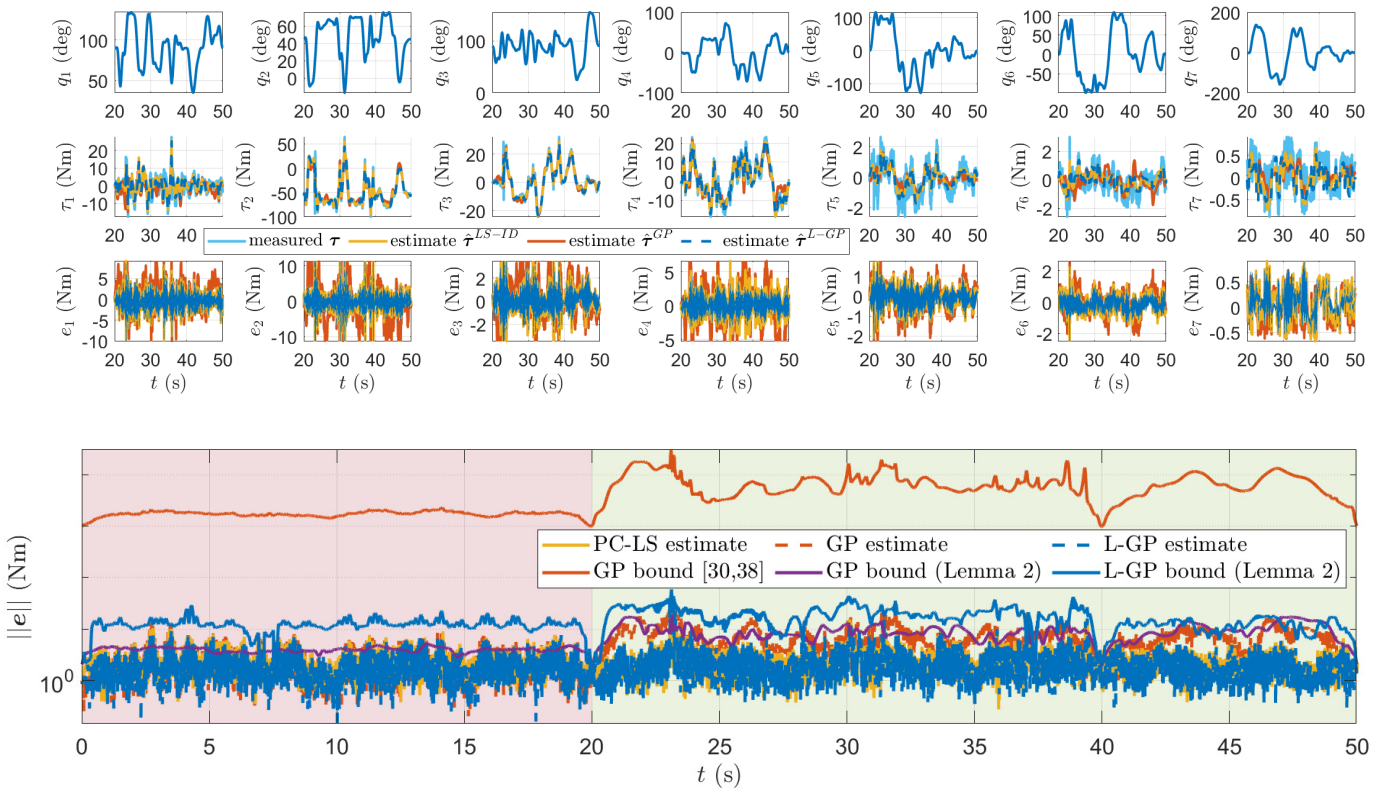

Fig. 9: Model identification of the KUKA IIWA (first 20 s) and validation using the next 30 s of an aggressively optimized excitation trajectory. Top: regression errors after identification. The proposed L-GP model has an overall RMS error of 1.0429 Nm, superior to 1.1208 Nm and 2.9108 Nm of LS-ID with LMIs [23] and standard GP, respectively. Bottom: model error norms and probabilistic bounds (GPs) evaluated for training (shaded red) and validation trajectories (shaded green).

δ	d	β	M_d	$L_{\boldsymbol{\tau}}$	$L_{\boldsymbol{K}_{\boldsymbol{\tau}}}$	$\|\boldsymbol{K}_{\boldsymbol{y}}^{-1}\|_F$	$\max\|\boldsymbol{K}_{\boldsymbol{\tau}}\|_F$	Δ	$\boldsymbol{K}_{O,P}^{\text{static}}$	$\boldsymbol{K}_{D,1\text{–}3}$	ϱ	α	ϱ^{PD}	α^{PD}
10^{-10}	10^{-15}	40.32	10^{335}	1.63e3	6.24e3	64.7289	3.3730e4	21.86	$40\boldsymbol{I}$	$20\boldsymbol{I}$	43.71	10	39.45	10.08

TABLE II: L-GP and MO parameter values.

adaptive observer gains are always lower than their static versions since $20\boldsymbol{I} \prec \boldsymbol{K}_{O,P}(\boldsymbol{\Sigma}_{\boldsymbol{\tau}}) \prec 40\boldsymbol{I}$ holds, cf. Tab. II. In practice, the variable L-GP-based PD-MO exhibits the highest precision for the disturbed scenario, which can also be confirmed theoretically by its smaller ultimate bound, or radius, ϱ^{PD}, and its slightly higher convergence rate α^{PD}, cf. Tab. II. For the undisturbed, free scenario, each MO variant also demonstrates incremental improvements as excepted, except for the P- versus PD-versions of adaptive L-GP-MOs. In this case, the presence of the additional derivative gain $\boldsymbol{K}_D$ seems to increase the MO's sensitivity to noise, an effect also discussed after Theorem 1, Sec. IV, in the context of high-gain observers, confirming the legitimation of the proposed adaptation scheme of decreasing the correction gain in areas of higher uncertainty.

VI. Conclusion

This article presents a probabilistic approach to disturbance observation with Momentum Observers (MOs) for uncertain mechanical systems. The framework is based on Lagrangian-Gaussian Processes (L-GPs), providing a data-driven yet physically consistent model whose covariance matrix estimate is leveraged to adapt the correction gain such that model errors are compensated by adapting to the uncertainty. Based on the derivation of probabilistic closed-form bounds of the error, exponential stability guarantees with user-definable convergence rates are provided. Various numerical and experimental results are presented, demonstrating the efficacy of the proposed methods. We are currently working on the experimental validation of our algorithms on soft robotic and rehabilitation systems. Furthermore, our future theoretical work will focus on unifying passivity-based control concepts with physically consistent machine learning.

Acknowledgments

This work was supported by the Consolidator Grant "Safe data-driven control for human-centric systems" (CO-MAN) of the European Research Council (ERC) and by the Horizon 2020 Research and Innovation Action project "Rehabilitation based on Hybrid neuroprosthesis" (ReHyb) of the European Union (EU) under grant agreement IDs 864686 and 871767,

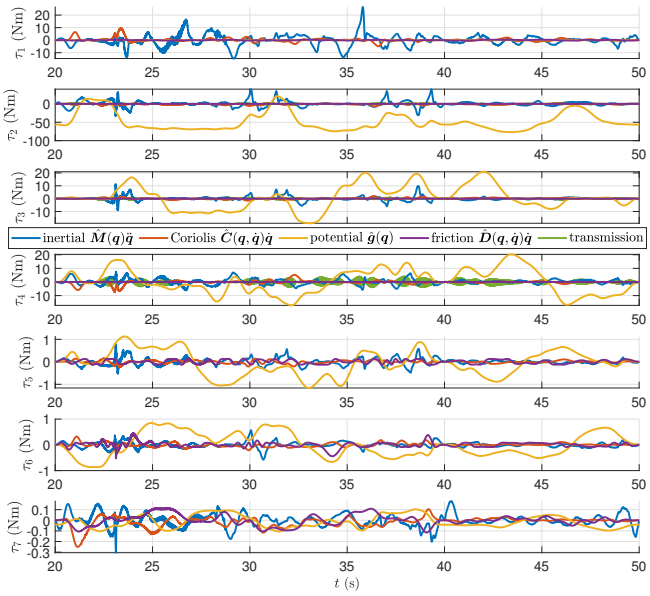

Fig. 10: L-GP model components for the KUKA IIWA evaluated over the validation trajectory. The model additionally includes another composite GP for each of the joints 2, 3, and 4, which have a periodic structure with velocity-dependent amplitude modulation.

respectively. The authors gratefully acknowledge the thoughtful comments and fruitful discussions with P. Budde gen. Dohmann, Chair of Information-oriented Control, Technical University of Munich. They also explicitly thank the reviewers for their helpful and constructive feedback.

Appendix A
Proof of Lemma 1: Probabilistic Multidimensional Error Bound on a Finite Set

Fixing $\boldsymbol{x} \in \mathcal{X}$ and conditioning on the noisy observations $\boldsymbol{y}_i$ from (4), the inputs $\boldsymbol{x}_i$ become deterministic and we can follow that $\boldsymbol{f}(\boldsymbol{x}) \sim \mathcal{N}(\boldsymbol{\mu_f}(\boldsymbol{x}), \boldsymbol{\Sigma_f}(\boldsymbol{x}))$. Now, for multivariate standard $\boldsymbol{\epsilon} \sim \mathcal{N}(\boldsymbol{0}, \boldsymbol{I})$, we compute with $\rho > 0$ that

$$\begin{aligned}\Pr\{\|\boldsymbol{\epsilon}\| > \rho\} &= (2\pi)^{-\frac{N}{2}} \int_{\|\boldsymbol{\epsilon}\|>\rho} e^{-\frac{\|\boldsymbol{\epsilon}\|^2}{2}} \boldsymbol{d\epsilon} \\ &= (2\pi)^{-\frac{N}{2}} \int_{\rho}^{\infty} \int_{0}^{2\pi} \int_{\boldsymbol{0}}^{\boldsymbol{\pi}} e^{-\frac{r^2}{2}} |\boldsymbol{J_\phi}| \boldsymbol{d\vartheta} d\varphi dr \\ &= \frac{\Gamma_{N/2}(\frac{\rho^2}{2})}{\gamma(\frac{N}{2})} := \tilde{\Gamma}_{N/2}(\tfrac{\rho^2}{2}), \end{aligned} \tag{44}$$

where we have transformed to N-dimensional spherical coordinates by $\boldsymbol{\epsilon} = \boldsymbol{\phi}(r, \varphi, \boldsymbol{\vartheta})$ with radius r, azimuth φ and elevation angles $\boldsymbol{\vartheta}$, and also used the identity

$$\int_0^{\pi} \sin^n(\vartheta_i) d\vartheta_i = \sqrt{\pi} \frac{\Gamma(\frac{n+1}{2})}{\Gamma(\frac{n}{2}+1)}, \quad \forall n \in \mathbb{N}.$$

The Jacobian $\boldsymbol{J_\phi} = \partial\boldsymbol{\phi}/\partial(r, \varphi, \boldsymbol{\vartheta})$ is required for the transformed differential volume element

$$\boldsymbol{d\epsilon} = r^{N-1} \sin^{N-2} \vartheta_1 \cdots \sin \vartheta_{N-2} dr \boldsymbol{d\vartheta} d\varphi .$$

Using (44) for $\rho = \beta$ and choosing $\boldsymbol{\epsilon} = \boldsymbol{R_f}^{-\top}(\boldsymbol{f} - \boldsymbol{\mu_f})$, where $\boldsymbol{R_f}$ stems from the Cholesky decomposition of the covariance $\boldsymbol{\Sigma_f} = \boldsymbol{R_f}^{\top} \boldsymbol{R_f}$, we obtain

$$\Pr\left\{ \|\boldsymbol{f} - \boldsymbol{\mu_f}\| > \beta \underline{\lambda}^{\frac{1}{2}}(\boldsymbol{\Sigma_f}) \right\} = \tilde{\Gamma}_{N/2}(\tfrac{\beta^2}{2}) .$$

Here, we have utilized $\|\boldsymbol{\epsilon}\|^2 \leq \bar{\lambda}(\boldsymbol{\Sigma_f}^{-1}) \|\boldsymbol{f} - \boldsymbol{\mu_f}\|^2$ along with $\bar{\lambda}(\boldsymbol{\Sigma_f}^{-1}) = \underline{\lambda}^{-1}(\boldsymbol{\Sigma_f})$. Finally, applying the union bound and taking the complement of the set, we conclude that

$$\|\boldsymbol{f}(\boldsymbol{x}) - \boldsymbol{\mu_f}(\boldsymbol{x})\| \leq \beta \underline{\lambda}^{\frac{1}{2}}(\boldsymbol{\Sigma_f}(\boldsymbol{x})) \quad \forall \boldsymbol{x} \in \mathcal{X}$$

holds with a probability of exactly $1 - |\mathcal{X}| \tilde{\Gamma}_{N/2}(\beta^2/2)$. Since $\tilde{\Gamma}_{N/2}(\beta^2/2) = \delta/|\mathcal{X}|$ due to (14), we arrive at (15).

Appendix B
Proof of Lemma 2: Extension of the Error Bound to a Compact Set

To begin with, we prove Lipschitz continuity of the posterior mean $\boldsymbol{\mu_f}$ and the bounded spectrum of the covariance matrix $\boldsymbol{\Sigma_f}$. The Euclidian distance between the estimate evaluated at two different points can be written as

$$\|\boldsymbol{\mu_f}(\boldsymbol{x}) - \boldsymbol{\mu_f}(\boldsymbol{x}')\| = \|(\boldsymbol{K}(\boldsymbol{x}, \boldsymbol{X}_D) - \boldsymbol{K}(\boldsymbol{x}', \boldsymbol{X}_D))\, \boldsymbol{\alpha}\|$$

with $\boldsymbol{\alpha} = \boldsymbol{K_y}^{-1}(\boldsymbol{y} - \boldsymbol{m})$. Using $\|\boldsymbol{Ax}\|_2 \leq \|\boldsymbol{A}\|_F \|\boldsymbol{x}\|_2$ due to the Cauchy-Schwarz inequality, along with $\|\boldsymbol{A}\|_F = \sqrt{\operatorname{tr}(\boldsymbol{A}\boldsymbol{A}^{\top})}$ and (19), we follow that

$$\|\boldsymbol{\mu_f}(\boldsymbol{x}) - \boldsymbol{\mu_f}(\boldsymbol{x}')\| \leq L_{\boldsymbol{K}} \sqrt{D} \|\boldsymbol{\alpha}\| \|\boldsymbol{x} - \boldsymbol{x}'\| ,$$

proving Lipschitz continuity of the multidimensional mean estimate $\boldsymbol{\mu_f}(\boldsymbol{x})$ with $L_{\boldsymbol{\mu}} = L_{\boldsymbol{K}} \sqrt{D} \|\boldsymbol{\alpha}\|$. Next, we investigate the continuity of the covariance $\boldsymbol{\Sigma_f}$. Applying the triangle inequality along with other fundamental properties of vector norms, we can write

$$\begin{aligned}\|\boldsymbol{\Sigma_f}(\boldsymbol{x}) - \boldsymbol{\Sigma_f}(\boldsymbol{x}')\|_F &\leq \|K(\boldsymbol{x}, \boldsymbol{x}) - K(\boldsymbol{x}', \boldsymbol{x}')\|_F \\ &+ \|K(\boldsymbol{x}, \cdot) - K(\boldsymbol{x}', \cdot)\|_F \|\boldsymbol{K_y}^{-1}\|_F \|K(\cdot, \boldsymbol{x}) + K(\cdot, \boldsymbol{x}')\|_F .\end{aligned}$$

Here, we have abbreviated $K(\boldsymbol{x}, \cdot) = K(\boldsymbol{x}, \boldsymbol{X}_D)$ for notational compactness. Due to Lipschitz continuity of the matrix kernel $\boldsymbol{K}$ according to (19), one can conclude that

$$\|\boldsymbol{\Sigma_f}(\boldsymbol{x}) - \boldsymbol{\Sigma_f}(\boldsymbol{x}')\|_F \leq s(\|\boldsymbol{x} - \boldsymbol{x}'\|) \tag{45}$$

with $s(d)$ given by (18). Now, consider any discretization $\mathcal{X}_d \subset \mathcal{X}$ of $\mathcal{X}$ by a finite number of $|\mathcal{X}_d|$ points. The distance for every $\boldsymbol{x} \in \mathcal{X}$ to the closest point $\boldsymbol{x}' \in \mathcal{X}_d$ is bounded by

$$\max_{\boldsymbol{x} \in \mathcal{X}} \min_{\boldsymbol{x}' \in \mathcal{X}_d} \|\boldsymbol{x} - \boldsymbol{x}'\| \leq d . \tag{46}$$

As a consequence, we can apply the result of Lemma 1 for $\beta(\delta, d) = \sqrt{2\Gamma^{-1}_{N/2}(\delta\gamma(N/2)/|\mathcal{X}_d(d)|)}$ and follow that

$$\|\boldsymbol{f}(\boldsymbol{x}') - \boldsymbol{\mu_f}(\boldsymbol{x}')\| \leq \beta(\delta, d) \underline{\lambda}^{\frac{1}{2}}(\boldsymbol{\Sigma_f}(\boldsymbol{x}'))$$

holds $\forall \boldsymbol{x}' \in \mathcal{X}_d$ with a probability of $1 - \delta$. Since $\Gamma_n(\rho)$ is monotonically decreasing, the covering number $M_d(\mathcal{X})$ can

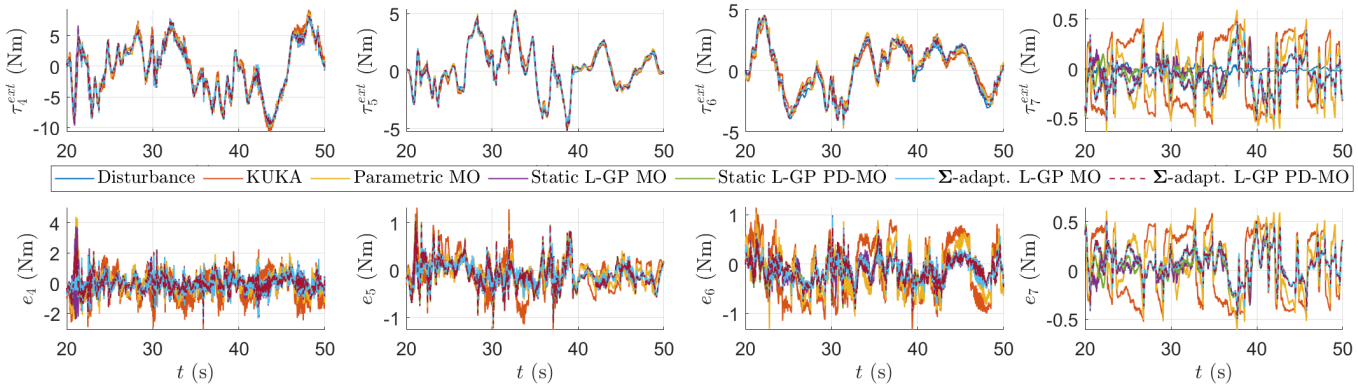

Fig. 11: MO estimates for a disturbance caused by the inertial forces of a Schunk gripper mounted to the robot's end-effector, illustrated for joints $n=4-7$. RMS values of estimation errors for joints $n=1-3$ of KUKA, parametric, static L-GP (PD-) and $\boldsymbol{\Sigma}$-adapt. L-GP (PD-)MO are 1.379, 1.303, 1.275 (1.000), and 1.131 (0.975) Nm with averaged STDs 1.147, 0.941, 0.883 (0.741), and 0.765 (0.695) Nm, respectively. The overall estimation accuracies are evaluated numerically in Tab. I.

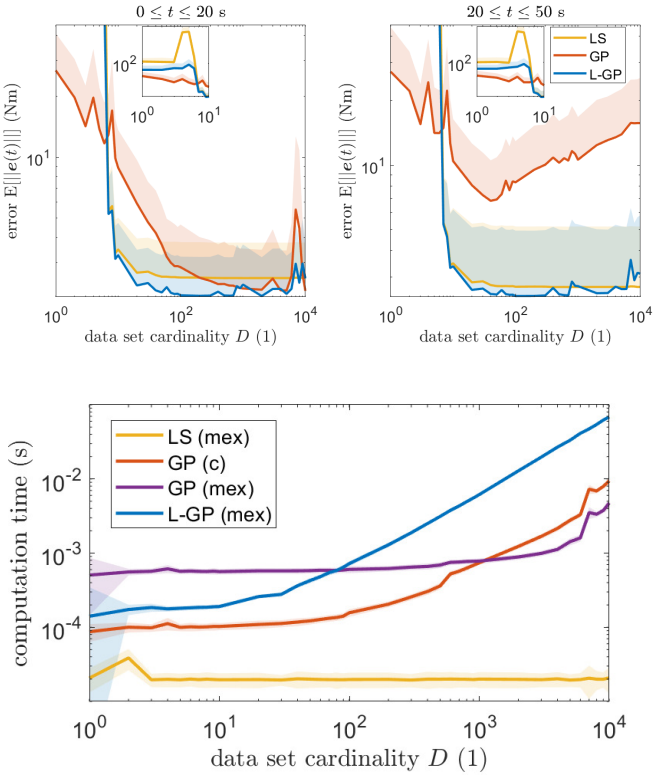

Fig. 12: Efficiency evaluation of LS, GP, and L-GP w.r.t. prediction errors in training (top left) and validation domains (top right), and computation timings (bottom) over data sizes. Solid lines depict mean values, shaded areas standard deviations.

be used w.l.o.g. to bound the minimum number of points needed to fulfill (46) on a grid. Finally, we leverage Weyl's inequality [54, Theorem III.2.1] along with the continuity of $\boldsymbol{f}(\boldsymbol{x})$, $\boldsymbol{\mu}_{\boldsymbol{f}}(\boldsymbol{x})$ and $\boldsymbol{\Sigma}_{\boldsymbol{f}}(\boldsymbol{x})$ to write

$$\begin{aligned}&\|\boldsymbol{f}(\boldsymbol{x}')-\boldsymbol{\mu}_{\boldsymbol{f}}(\boldsymbol{x}')\|+\|\boldsymbol{f}(\boldsymbol{x})-\boldsymbol{f}(\boldsymbol{x}')\|+\|\boldsymbol{\mu}_{\boldsymbol{f}}(\boldsymbol{x})-\boldsymbol{\mu}_{\boldsymbol{f}}(\boldsymbol{x}')\|\\&\leq\beta(\delta,d)\sqrt{\underline{\lambda}(\boldsymbol{\Sigma}_{\boldsymbol{f}}(\boldsymbol{x}))+\bar{\lambda}(\boldsymbol{\Sigma}_{\boldsymbol{f}}(\boldsymbol{x}')-\boldsymbol{\Sigma}_{\boldsymbol{f}}(\boldsymbol{x}))}+(L_{\boldsymbol{f}}+L_{\boldsymbol{\mu}})d\,.\end{aligned}\tag{47}$$

Applying the triangle inequality to the left and using (45) combined with $\bar{\lambda}(\cdot)\leq\|\cdot\|_F$ on the right, we finish the proof.

Appendix C
Multidimensional Derivative Error Bound

For a bound on the time derivative of the estimation error, we first make use of the chain rule to write

$$\dot{\boldsymbol{f}}(\boldsymbol{x})-\dot{\boldsymbol{\mu}}_{\boldsymbol{f}}(\boldsymbol{x})=\tfrac{\partial(\boldsymbol{f}-\boldsymbol{\mu}_{\boldsymbol{f}})}{\partial\boldsymbol{x}}\dot{\boldsymbol{x}}\,.\tag{48}$$

Taking the norm and applying the Cauchy-Schwarz and triangle inequalities gives

$$\|\dot{\boldsymbol{f}}-\dot{\boldsymbol{\mu}}_{\boldsymbol{f}}\|\leq\left\|\tfrac{\partial(\boldsymbol{f}-\boldsymbol{\mu}_{\boldsymbol{f}})}{\partial\boldsymbol{x}}\right\|_F\|\dot{\boldsymbol{x}}\|\leq(L_{\boldsymbol{f}}+L_{\boldsymbol{\mu}})\|\dot{\boldsymbol{x}}\|\,.\tag{49}$$

Thus, we have already arrived at a conservative deterministic bound based on Lipschitz continuity. For a more precise probabilistic bound, we leverage the linearity of GPs as well as that of differentiation to denote

$$\operatorname{vec}\left(\tfrac{\partial\boldsymbol{f}}{\partial\boldsymbol{x}}\right)\sim\mathcal{GP}\left(\operatorname{vec}\left(\tfrac{\partial\boldsymbol{m}}{\partial\boldsymbol{x}}\right),\operatorname{vec}\left(\tfrac{\partial}{\partial\boldsymbol{x}}\right)\boldsymbol{K}(\boldsymbol{x},\boldsymbol{x}')\operatorname{vec}^{\top}\left(\tfrac{\partial}{\partial\boldsymbol{x}'}\right)\right)\,.$$

Using $\|\cdot\|_F=\|\operatorname{vec}(\cdot)\|_2$ as well as the result of Lemma 2, we follow $\forall\boldsymbol{x}\in\mathcal{X}$ that

$$\Pr\left\{\|\dot{\boldsymbol{f}}(\boldsymbol{x})-\dot{\boldsymbol{\mu}}_{\boldsymbol{f}}(\boldsymbol{x})\|\leq\varrho(\boldsymbol{x},\delta,d)\|\dot{\boldsymbol{x}}\|\right\}=1-\delta\,,\tag{50}$$

having introduced for $\tilde{\boldsymbol{f}}(\boldsymbol{x})\coloneqq\operatorname{vec}(\partial\boldsymbol{f}/\partial\boldsymbol{x})$ the radius scale

$$\varrho(\boldsymbol{x},\delta,d)=\beta(\delta,d)\sqrt{\underline{\lambda}(\boldsymbol{\Sigma}_{\tilde{\boldsymbol{f}}}(\boldsymbol{x}))+\tilde{s}(d)}+(L_{\tilde{\boldsymbol{f}}}+L_{\tilde{\boldsymbol{\mu}}})d\,.\tag{51}$$

This is the author's version of an article published in the IEEE Transactions on Robotics (T-RO).
The final published paper can be found at DOI: 10.1109/TRO.2024.3366818

APPENDIX D
LIPSCHITZ APPROXIMATION OF LAGRANGIAN SYSTEMS

For a compact derivation of a Lipschitz constant $L_{\boldsymbol{\tau}}$ for Lagrangian systems such that

$$\|\boldsymbol{\tau}(\boldsymbol{x}) - \boldsymbol{\tau}(\boldsymbol{y})\|_2 \leq L_{\boldsymbol{\tau}} \|\boldsymbol{x} - \boldsymbol{y}\|_2 \,, \tag{52}$$

we use the following approximate multidimensional extension of the mean value theorem

$$\|\boldsymbol{f}(\boldsymbol{x}) - \boldsymbol{f}(\boldsymbol{y})\|_2 \leq \left(\max_{\boldsymbol{z} \in [\boldsymbol{x}, \boldsymbol{y}]} \| \tfrac{\partial \boldsymbol{f}}{\partial \boldsymbol{z}} \|_F \right) \|\boldsymbol{y} - \boldsymbol{x}\|_2 \tag{53}$$

with differentiable $\boldsymbol{f} \colon \mathbb{R}^M \to \mathbb{R}^N$ on an open set containing the two points $\boldsymbol{x}, \boldsymbol{y} \in \mathbb{R}^M$. Applying (53) to the total torque acting upon the system, we first compute

$$\dot{\boldsymbol{\tau}} = \boldsymbol{M}\, \ddot{\boldsymbol{q}} + (\dot{\boldsymbol{M}} + \boldsymbol{C} + \boldsymbol{D}) \ddot{\boldsymbol{q}} + (\dot{\boldsymbol{C}} + \tfrac{\partial^2 V}{\partial \boldsymbol{q}^2} + \dot{\boldsymbol{D}}) \dot{\boldsymbol{q}} \,. \tag{54}$$

Rewriting $\dot{\boldsymbol{\tau}} = \frac{\partial \boldsymbol{\tau}}{\partial \boldsymbol{x}} \dot{\boldsymbol{x}}$ and reformulating (54), we obtain $L_{\boldsymbol{\tau}} = \max_{\boldsymbol{z} \in [\boldsymbol{x}, \boldsymbol{y}]} \| \frac{\partial \boldsymbol{\tau}}{\partial \boldsymbol{z}} \|_F$ with

$$\tfrac{\partial \boldsymbol{\tau}}{\partial \boldsymbol{x}} = \begin{bmatrix} \dot{\boldsymbol{C}} + \tfrac{\partial^2 V}{\partial \boldsymbol{q}^2} + \dot{\boldsymbol{D}} & \dot{\boldsymbol{M}} + \boldsymbol{C} + \boldsymbol{D} & \boldsymbol{M} \end{bmatrix} . \tag{55}$$

Note that $L_{\boldsymbol{\tau}}$ can be estimated and simplified even further by exploiting fundamental properties of vector norms such as submultiplicativity and the triangular inequality.

APPENDIX E
QUADRATIC FUNCTION SPACE

The deterministic preservation of the quadratic form of kinetic and elastic energy GPs can be shown by analyzing the covariance kernel structures as in [41, Lemma 1], or via the RKHS associated with the kernel (12). Let us reformulate

$$\begin{aligned} T(\cdot, \dot{\boldsymbol{q}}) &= \tfrac{1}{2} \mathrm{tr} \left(\boldsymbol{M} \dot{\boldsymbol{q}} \dot{\boldsymbol{q}}^\top \right) = \tfrac{1}{2} \mathrm{vec}(\boldsymbol{M})^\top \mathrm{vec}(\dot{\boldsymbol{q}} \dot{\boldsymbol{q}}^\top) \\ &= \tfrac{1}{2} \mathrm{vec}(\boldsymbol{M})^\top (\dot{\boldsymbol{q}} \otimes \dot{\boldsymbol{q}}) \,, \end{aligned}$$

where we have subsequently exploited the cyclic trace property, the compatibility of vectorization with inner products, and finally, the relationship between Kronecker and matrix products via vectorization. Consider now the Hilbert space $\mathcal{H}_{\text{quad}}$ comprised of real quadratic functions, defined on the index set $\Xi = \mathbb{R}^N$, and constructed via the linear combination of N^2 basis functions

$$\mathcal{H}_{\text{quad}} = \left\{ \boldsymbol{F} \in \mathbb{R}^{N \times N} \,\middle|\, f(\dot{\boldsymbol{q}}) = \mathrm{vec}(\boldsymbol{F})^\top \boldsymbol{\phi}(\dot{\boldsymbol{q}}) \,,\ \forall \dot{\boldsymbol{q}} \in \mathbb{R}^N \right\} \tag{56}$$

with feature map $\boldsymbol{\phi} \colon \Xi \to \mathcal{F}$ chosen as $\boldsymbol{\phi}(\dot{\boldsymbol{q}}) = \frac{1}{2} (\dot{\boldsymbol{q}} \otimes \dot{\boldsymbol{q}})$. We endow $\mathcal{H}_{\text{quad}}$ with the inner product $\langle \cdot, \cdot \rangle_{\mathcal{H}_{\text{quad}}}$ defined as

$$\langle f,\, g \rangle_{\mathcal{H}_{\text{quad}}} = \mathrm{vec}(\boldsymbol{F})^\top \mathrm{diag}^{-1} \left[\mathrm{vec}(\boldsymbol{\Theta}_{\boldsymbol{M}}) \right] \mathrm{vec}(\boldsymbol{G}) \,,$$

with the function $g(\dot{\boldsymbol{q}}) = \mathrm{vec}(\boldsymbol{G})^\top \boldsymbol{\phi}(\dot{\boldsymbol{q}})$, which always exists since $\mathrm{vec}(\boldsymbol{\Theta}_{\boldsymbol{M}}) = (\boldsymbol{I} \otimes \boldsymbol{R}_{\boldsymbol{M}}^\top) \mathrm{vec}(\boldsymbol{R}_{\boldsymbol{M}}) > \boldsymbol{0}$ holds element-wise, i.e., since $\boldsymbol{R}_{\boldsymbol{M}} > \boldsymbol{0}$. Also, using the trace and vectorization operators as well as the mixed product property of Kronecker and Hadamard products, we transform (12) to

$$k_T(\cdot, \dot{\boldsymbol{q}}, \cdot, \dot{\boldsymbol{q}}') = \boldsymbol{\phi}(\dot{\boldsymbol{q}})^\top \mathrm{diag}(\mathrm{vec}(\boldsymbol{\Theta}_{\boldsymbol{M}}(\cdot, \cdot))) \boldsymbol{\phi}(\dot{\boldsymbol{q}}') \,.$$

Let the feature space $\mathcal{F}$ be a Hilbert space with inner product

$$\langle \boldsymbol{\phi},\, \boldsymbol{\psi} \rangle_{\mathcal{F}} = \boldsymbol{\phi}^\top \mathrm{diag}(\mathrm{vec}(\boldsymbol{\Theta}_{\boldsymbol{M}})) \boldsymbol{\psi} \,.$$

Thus, the inner product of the feature map with itself constructs the kernel $k_T = \langle \boldsymbol{\phi}(\dot{\boldsymbol{q}}),\, \boldsymbol{\phi}(\dot{\boldsymbol{q}}') \rangle_{\mathcal{F}}$. For every $\dot{\boldsymbol{q}}$, k_T as a function of $\dot{\boldsymbol{q}}'$ belongs to $\mathcal{H}_{\text{quad}}$ since

$$k_T(\cdot, \cdot, \cdot, \dot{\boldsymbol{q}}') = \tfrac{1}{2} \dot{\boldsymbol{q}}'^\top \boldsymbol{\mathcal{K}} \dot{\boldsymbol{q}}' = \mathrm{vec}(\boldsymbol{\mathcal{K}})^\top \boldsymbol{\phi}(\dot{\boldsymbol{q}}')$$

with $\boldsymbol{\mathcal{K}} = \frac{1}{2} \dot{\boldsymbol{q}} \dot{\boldsymbol{q}}^\top \circ \boldsymbol{\Theta}(\boldsymbol{q}, \boldsymbol{q}')$. Furthermore, the inner product of $f \in \mathcal{H}_{\text{quad}}$ with $k_T(\cdot, \cdot, \cdot, \dot{\boldsymbol{q}})$ gives

$$\langle f(\cdot),\, k_T(\cdot, \cdot, \cdot, \dot{\boldsymbol{q}}) \rangle_{\mathcal{H}_{\text{quad}}} = \mathrm{vec}(\boldsymbol{F})^\top \mathrm{vec}(\tfrac{1}{2} \dot{\boldsymbol{q}} \dot{\boldsymbol{q}}^\top) = f(\dot{\boldsymbol{q}}) \,,$$

showing the reproducing property of the kernel. Thus, we conclude that the Hilbert space $\mathcal{H}_{\text{quad}}$ of real quadratic functions (56) is an RKHS spanned uniquely by (12).

REFERENCES

[1] N. Hogan, "Impedance control: An approach to manipulation," in *1984 American Control Conference*, 1984, pp. 304–313.

[2] A. De Santis, B. Siciliano, A. De Luca, and A. Bicchi, "An atlas of physical human–robot interaction," *Mechanism and Machine Theory*, vol. 43, no. 3, pp. 253–270, 2008.

[3] C. Della Santina, M. G. Catalano, and A. Bicchi, *Soft Robots*. Berlin, Heidelberg: Springer Berlin Heidelberg, 2020, pp. 1–15.

[4] B. Vanderborght et al, "Variable impedance actuators: A review," *Robotics and Autonomous Systems*, vol. 61, no. 12, pp. 1601–1614, 2013.

[5] K. Anam and A. A. Al-Jumaily, "Active exoskeleton control systems: State of the art," *Procedia Engineering*, vol. 41, pp. 988–994, 2012, international Symposium on Robotics and Intelligent Sensors 2012.

[6] D. Rus and M. T. Tolley, "Design, fabrication and control of soft robots," *Nature*, vol. 521, no. 7553, pp. 467–475, 2015.

[7] L. Marchal-Crespo and D. J. Reinkensmeyer, "Review of control strategies for robotic movement training after neurologic injury," *Journal of NeuroEngineering and Rehabilitation*, vol. 6, no. 1, p. 20, 2009.

[8] L. Sentis, J. Park, and O. Khatib, "Compliant control of multicontact and center-of-mass behaviors in humanoid robots," *IEEE Transactions on Robotics*, vol. 26, no. 3, pp. 483–501, 2010.

[9] C. D. Santina, R. K. Katzschmann, A. Bicchi, and D. Rus, "Model-based dynamic feedback control of a planar soft robot: trajectory tracking and interaction with the environment," *The International Journal of Robotics Research*, vol. 39, no. 4, pp. 490–513, 2020.

[10] A. Bicchi, M. A. Peshkin, and J. E. Colgate, *Safety for Physical Human–Robot Interaction*. Berlin, Heidelberg: Springer Berlin Heidelberg, 2008, pp. 1335–1348.

[11] S. Haddadin, A. De Luca, and A. Albu-Schäffer, "Robot collisions: A survey on detection, isolation, and identification," *IEEE Transactions on Robotics*, vol. 33, no. 6, pp. 1292–1312, 2017.

[12] A. de Luca and R. Mattone, "Sensorless robot collision detection and hybrid force/motion control," in *Proceedings of the 2005 IEEE International Conference on Robotics and Automation*, 2005, pp. 999–1004.

[13] A. De Luca, A. Albu-Schaffer, S. Haddadin, and G. Hirzinger, "Collision detection and safe reaction with the dlr-iii lightweight manipulator arm," in *2006 IEEE/RSJ International Conference on Intelligent Robots and Systems*, 2006, pp. 1623–1630.

[14] K. Rath, C. G. Albert, B. Bischl, and U. von Toussaint, "Symplectic gaussian process regression of maps in hamiltonian systems," *Chaos: An Interdisciplinary Journal of Nonlinear Science*, vol. 31, no. 5, p. 053121, 2021.

[15] T. Beckers, J. Seidman, P. Perdikaris, and G. J. Pappas, "Gaussian process port-hamiltonian systems: Bayesian learning with physics prior," in *2022 IEEE 61st Conference on Decision and Control (CDC)*, 2022, pp. 1447–1453.

[16] T. P. Duong and N. A. Atanasov, "Hamiltonian-based neural ode networks on the se(3) manifold for dynamics learning and control," in *Robotics: Science and Systems 2021*, 2021.

[17] S. Greydanus, M. Dzamba, and J. Yosinski, "Hamiltonian neural networks," in *Advances in Neural Information Processing Systems*, vol. 32. Curran Associates, Inc., 2019.

[18] R. Grandia, D. Pardo, and J. Buchli, "Contact invariant model learning for legged robot locomotion," *IEEE Robotics and Automation Letters*, vol. 3, no. 3, pp. 2291–2298, 2018.

[19] L. Rath, A. R. Geist, and S. Trimpe, "Using physics knowledge for learning rigid-body forward dynamics with gaussian process force priors," in *Proceedings of the 5th Conference on Robot Learning*, ser. Proceedings of Machine Learning Research, vol. 164. PMLR, 08–11 Nov 2022, pp. 101–111.

[20] A. Geist and S. Trimpe, "Learning constrained dynamics with gauss' principle adhering gaussian processes," in *Proceedings of the 2nd Conference on Learning for Dynamics and Control*, ser. Proceedings of Machine Learning Research, vol. 120. PMLR, 10–11 Jun 2020, pp. 225–234.

[21] A. R. Geist and S. Trimpe, "Structured learning of rigid-body dynamics: A survey and unified view from a robotics perspective," *GAMM-Mitteilungen*, vol. 44, no. 2, p. e202100009, 2021.

[22] L. Ljung, *System Identification: Theory for the User*, 2nd ed., ser. PTR Prentice Hall Information and System Sciences. Pearson, 1998.

[23] P. M. Wensing, S. Kim, and J.-J. E. Slotine, "Linear matrix inequalities for physically consistent inertial parameter identification: A statistical perspective on the mass distribution," *IEEE Robotics and Automation Letters*, vol. 3, no. 1, pp. 60–67, 2018.

[24] Q. Leboutet, J. Roux, A. Janot, J. R. Guadarrama-Olvera, and G. Cheng, "Inertial parameter identification in robotics: A survey," *Applied Sciences*, vol. 11, no. 9, 2021.

[25] C. Armanini, F. Boyer, A. T. Mathew, C. Duriez, and F. Renda, "Soft robots modeling: A structured overview," *IEEE Transactions on Robotics*, vol. 39, no. 3, pp. 1728–1748, 2023.

[26] M. P. Deisenroth, D. Fox, and C. E. Rasmussen, "Gaussian processes for data-efficient learning in robotics and control," *IEEE Transactions on Pattern Analysis and Machine Intelligence*, vol. 37, no. 2, pp. 408–423, 2015.

[27] C. E. Rasmussen and C. K. I. Williams, *Gaussian Processes for Machine Learning*. The MIT Press, 2006.

[28] N. Srinivas, A. Krause, S. M. Kakade, and M. W. Seeger, "Information-theoretic regret bounds for gaussian process optimization in the bandit setting," *IEEE Transactions on Information Theory*, vol. 58, no. 5, pp. 3250–3265, 2012.

[29] J. Umlauft and S. Hirche, "Feedback linearization based on gaussian processes with event-triggered online learning," *IEEE Transactions on Automatic Control*, 2020.

[30] T. Beckers, D. Kulić, and S. Hirche, "Stable gaussian process based tracking control of euler–lagrange systems," *Automatica*, vol. 103, pp. 390–397, 2019.

[31] C. Fiedler, C. W. Scherer, and S. Trimpe, "Learning-enhanced robust controller synthesis with rigorous statistical and control-theoretic guarantees," in *2021 60th IEEE Conference on Decision and Control (CDC)*, 2021, pp. 5122–5129.

[32] S. Reece and S. Roberts, "An introduction to gaussian processes for the kalman filter expert," in *2010 13th International Conference on Information Fusion*, 2010, pp. 1–9.

[33] C.-A. Cheng and H.-P. Huang, "Learn the lagrangian: A vector-valued rkhs approach to identifying lagrangian systems," *IEEE Transactions on Cybernetics*, vol. 46, no. 12, pp. 3247–3258, 2016.

[34] S. Ober-Blöbaum and C. Offen, "Variational learning of euler–lagrange dynamics from data," *Journal of Computational and Applied Mathematics*, vol. 421, p. 114780, 2023.

[35] T. G. Thuruthel, B. Shih, C. Laschi, and M. T. Tolley, "Soft robot perception using embedded soft sensors and recurrent neural networks," *Science Robotics*, vol. 4, no. 26, p. eaav1488, 2019.

[36] D. Lim, D. Kim, and J. Park, "Momentum observer-based collision detection using lstm for model uncertainty learning," in *2021 IEEE International Conference on Robotics and Automation (ICRA)*, 2021, pp. 4516–4522.

[37] C. D. Santina, R. L. Truby, and D. Rus, "Data–driven disturbance observers for estimating external forces on soft robots," *IEEE Robotics and Automation Letters*, vol. 5, no. 4, pp. 5717–5724, 2020.

[38] A. Lederer, J. Umlauft, and S. Hirche, "Uniform error bounds for gaussian process regression with application to safe control," in *Advances in Neural Information Processing Systems*, vol. 32. Curran Associates, Inc., 2019.

[39] S. R. Chowdhury and A. Gopalan, "On kernelized multi-armed bandits," in *Proceedings of the 34th International Conference on Machine Learning*, vol. 70. PMLR, 06–11 Aug 2017, pp. 844–853.

[40] C. Fiedler, C. W. Scherer, and S. Trimpe, "Practical and rigorous uncertainty bounds for gaussian process regression," *Proceedings of the AAAI Conference on Artificial Intelligence*, vol. 35, no. 8, pp. 7439–7447, May 2021. [Online]. Available: https://ojs.aaai.org/index.php/AAAI/article/view/16912

[41] G. Evangelisti and S. Hirche, "Physically consistent learning of conservative lagrangian systems with gaussian processes," in *2022 IEEE 61st Conference on Decision and Control (CDC)*, 2022, pp. 4078–4085.

[42] A. D. L. Francesco Bullo, *Geometric Control of Mechanical Systems: Modeling, Analysis, and Design for Simple Mechanical Control Systems*, 1st ed., ser. Texts in Applied Mathematics. Springer New York, NY, 2005.

[43] C. P. P. Herbert Goldstein and J. L. Safko, *Classical Mechanics*, 3rd ed. Pearson, 2002.

[44] K. M. de Payrebrune and O. M. O'Reilly, "On constitutive relations for a rod-based model of a pneu-net bending actuator," *Extreme Mechanics Letters*, vol. 8, pp. 38–46, 2016, nanomechanics: Bridging Spatial and Temporal Scales.

[45] R. M. Murray, Z. Li, and S. S. Sastry, *A Mathematical Introduction to Robotic Manipulation*. CRC Press, 1994.

[46] M. Raissi, P. Perdikaris, and G. E. Karniadakis, "Inferring solutions of differential equations using noisy multi-fidelity data," *Journal of Computational Physics*, vol. 335, pp. 736–746, 2017.

[47] E. Solak, R. Murray-smith, W. Leithead, D. Leith, and C. Rasmussen, "Derivative observations in gaussian process models of dynamic systems," in *Advances in Neural Information Processing Systems*, vol. 15. MIT Press, 2002.

[48] M. A. Álvarez, L. Rosasco, and N. D. Lawrence, "Kernels for vector-valued functions: A review," *Foundations and Trends® in Machine Learning*, vol. 4, no. 3, pp. 195–266, 2012.

[49] C. G. Albert and K. Rath, "Gaussian process regression for data fulfilling linear differential equations with localized sources," *Entropy*, vol. 22, no. 2, 2020.

[50] W. M. Wojewoda Jerzy, Stefański Andrzej and K. Tomasz, "Hysteretic effects of dry friction: modelling and experimental studies," *Phil. Trans. R. Soc. A.*, vol. 366, pp. 747–765, 2007.

[51] J. Mercer, "Xvi. functions of positive and negative type, and their connection the theory of integral equations," *Philosophical Transactions of the Royal Society of London*, pp. 415–446, 1909.

[52] I. Steinwart, "On the influence of the kernel on the consistency of support vector machines," *J. Mach. Learn. Res.*, vol. 2, pp. 67–93, mar 2002.

[53] S. Shalev-Shwartz and S. Ben-David, *Understanding Machine Learning: From Theory to Algorithms*. Cambridge University Press, 2014.

[54] R. Bhatia, *Matrix Analysis*, 1st ed., ser. Graduate Texts in Mathematics. Springer, New York, NY, 1997.

[55] M. Corless, "Guaranteed rates of exponential convergence for uncertain systems," *Journal of Optimization Theory and Applications*, vol. 64, no. 3, pp. 481–494, 1990.

[56] H. K. Khalil, *Nonlinear Systems*, 3rd ed. Prentice Hall, 2002.

[57] W. Lohmiller and J.-J. E. Slotine, "On contraction analysis for non-linear systems," *Automatica*, vol. 34, no. 6, pp. 683–696, 1998.

[58] KUKA, "Lbr iiwa 7 r800, lbr iiwa 14r820 specification," 2015.

[59] M. V. Mark W. Spong, *Robot Dynamics and Control*. Wiley, 1991.

[60] C. Della Santina, R. K. Katzschmann, A. Biechi, and D. Rus, "Dynamic control of soft robots interacting with the environment," in *2018 IEEE International Conference on Soft Robotics (RoboSoft)*, 2018, pp. 46–53.

[61] R. S. Penning and M. R. Zinn, "A combined modal-joint space control approach for continuum manipulators," *Advanced Robotics*, vol. 28, no. 16, pp. 1091–1108, 2014.

[62] V. Chawda and G. Niemeyer, "Toward torque control of a kuka lbr iiwa for physical human-robot interaction," in *2017 IEEE/RSJ International Conference on Intelligent Robots and Systems (IROS)*, 2017, pp. 6387–6392.

Giulio Evangelisti received the B.Sc. and M.Sc. degrees in Electrical Engineering and Information Technology from the Technical University of Munich (TUM), Germany, in 2017 and 2019, respectively. From 2017 to 2018, he was part of the signal generator department of the measurement technology division at Rohde & Schwarz GmbH & Co. KG, Munich, and from 2019 to 2020 a full-time control engineer at Blickfeld GmbH, Munich. Since January 2021, he has been a Ph.D. candidate at the Chair of Information-oriented Control, TUM School of Computation, Information and Technology. His current research interests include the stability of data-driven control systems, physically consistent machine learning, nonlinear and passivity-based control, and robotics.

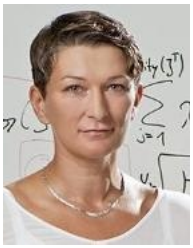

Sandra Hirche holds the TUM Liesel Beckmann Distinguished Professorship and heads the Chair of Information-oriented Control in the Faculty of Electrical and Computer Engineering at Technical University of Munich (TUM), Germany (since 2013). She received the diploma engineer degree in Aeronautical and Aerospace Engineering in 2002 from the Technical University Berlin, Germany, and the Doctor of Engineering degree in Electrical and Computer Engineering in 2005 from the Technische Universität München, Munich, Germany. From 2005-2007 she has been a PostDoc Fellow of the Japanese Society for the Promotion of Science at the Fujita Laboratory at Tokyo Institute of Technology, Japan. Prior to her present appointment she has been an Associate Professor at TUM. Her main research interests include learning, cooperative, and distributed control with application in human-robot interaction, multi-robot systems, and general robotics. She has published more than 200 papers in international journals, books, and refereed conferences.